# X-ray sensitivity and resolution of hybrid perovskite X-ray imaging detectors

**Afazul Hoq**

**A Thesis**

**in**

**The Department**

**of**

**Electrical and Computer Engineering**

**Presented in Partial Fulfillment of the Requirements for the Degree of**

**Master of Applied Science (Electrical & Computer Engineering) at**

**Concordia University**

**Montreal, Quebec, Canada**

**April 2022**

# CONCORDIA UNIVERSITY

# SCHOOL OF GRADUATE STUDIES

This is to certify that the thesis prepared

By: Afazul Hoq

Entitled: X-ray sensitivity and resolution of hybrid perovskite X-ray imaging detectors

and submitted in partial fulfillment of the requirements for the degree of

**Master of Applied Science (Electrical & Computer Engineering)**

complies with the regulations of this university and meets the accepted standards with respect to originality and quality.

Signed by the final examining committee:

_____Chair and Internal Examiner

Dr. Mojtaba Kahrizi

_____ External Examiner

Dr. A.K. Waizuddin Ahmed

_____ Supervisor

Dr. M. Z. Kabir

Approved by: _____

Dr. Yousef R. Shayan, Chair

Department of Electrical and Computer Engineering

_____20___ _____

Dr. Mourad Debbabi, Dean

Gina Cody School Engineering and Computer Science

# ABSTRACT

## X-ray sensitivity and resolution of hybrid perovskite X-ray imaging detectors

Afazul Hoq

The flat panel detectors (FPD) are digital detectors that are utilized extensively in medical applications such as digital chest radiography and mammography. The detectors are subjected to electromagnetic radiation to produce digital images of human internal organs. The electromagnetic radiation (X-ray) generates electron-hole pair in the photoconductor layer. The photogenerated electron-hole pairs drift under the influence of an applied electric field and generate a photocurrent. The performance of detectors essentially depends upon the selection of photoconductors. Over the years, x-ray imaging detectors with a-Se are widely used because of its uniform deposition, moderate sensitivity, good image resolution, and considerably low dark current. However, the medical diagnostic applications of a-Se get restricted due to high ionization energy, relatively low absorption coefficient. The hybrid organic perovskite has ionization energy an order lower than a-Se, good absorption coefficient, and superior charge transport properties that make hybrid organic perovskite a suitable candidate to replace the commercially used a-Se detectors.

In this thesis, the sensitivity of hybrid organic perovskite-based detectors under different operation conditions has been critically analyzed. The change of sensitivity is not significant for single exposure medical diagnostic X-ray applications. However, the sensitivity of perovskite-based detectors starts to deteriorate due to repeated and large exposures. The electric field across the photoconductor thickness becomes non-uniform due to the accumulation of trapped charge carriers. The loss of carriers due to bimolecular recombination leads to a decline of charge collection efficiency which results in an overall reduction of sensitivity. A physics-based model has been implemented to analyze the x-ray sensitivity under repeated exposures and different operating conditions. The model included the coupled continuity, trapping rate, and Poisson's and these equations are solved simultaneously. All possible recombination processes and traps are considered in the model with appropriate assumptions. The results of the model are compared with experimental values. It is vital to investigate the loss of image resolution of a hybrid organic

perovskite detector. The loss of image resolution of organic perovskite material is mainly due to k-fluorescence reabsorption, charge carrier trapping, and charge carrier diffusion. A physics-based model has been used to study the reduction of the modulation transfer function for different spatial frequencies. The work in this thesis identifies the main reasons for the ghosting effect under repeated exposures and the loss of image resolutions.

# ACKNOWLEDGEMENT

I would like to extend my deepest gratitude and appreciation to my thesis supervisor Dr. Zahangir Kabir for his relentless guidance, encouragement, and financial support throughout the progress of the research work. Without his constant support and supervision, accomplishing this thesis would not have been entirely possible.

I would like to thank Dr. A.K. Waizuddin Ahmed for his encouragement and appreciation. I would like to thank Mithun Roy for his encouragement and helpful discussions, guidance, and suggestions. I am also grateful to other research members including Iqbal Preet Singh, Salman Moazzem Arnab, Dhilippan Mamsapuram Panneerselvam, and Mauricio Buitrago. I would like to express my appreciation to NSERC and Concordia University for the financial support I have received

Finally, I would like to thank my parents, my grandmother, and my elder brother Irteza Hoq for their continuous moral support in every aspect of my life.

## Table of Contents

# List of Figures

**Figure 2.9**: It demonstrates X-rays are incident along the line (along z' in the figure) over the pixel electrodes of the image detector, where the y'z' forms a plane of the image detector. The X-rays incident upon the y' represents the delta function. The output charge signal along the line y' is spread out presents the LSF(y').

**Figure 2.10**: a) Pixel aperture width and pixel pitch. b) $MTF_a(f')$ as a function spatial frequency $f'$. The first zero of MTF($f'$) occurs at 1/a'.

**Figure 2.11**: Demonstrates the characteristics of Image lag and Ghosting taking place immediately after the exposure over a rectangular area. a) A dark image is obtained immediately after the X-ray exposure; Image lag is seen due to the interference of X-ray image of previous exposure. b) A shadow of impression is acquired image is visible in subsequent uniform exposure. Ghosting arises due to the reduction of pixel sensitivity in particular areas subjected to subsequent uniform exposure.

**Figure 3.1:** Relative X-ray sensitivity versus accumulated dose.

**Figure 3.2:** The concentration distributions of steady-state free and trapped carriers at the end of cumulative exposure of 0.5 mGy across the photoconductor layer (normalized distance = $x/L$).

**Figure 3.3:** The normalized electric field distribution as a function of cumulative dose.

**Figure 3.4:** Collected charge as a function of dose per exposure. An 800 μm thick $MAPbI_3$ X-ray detector with applied electric field $F_0$ = 0.2 V/μm under X-ray exposure at 70 kVp with 2.5 mm Al filtration.

**Figure 3.5:** The trapped carrier concentrations after exposures of 1 mGy (solid lines) and 12 mGy (dashed lines). Normalized distance = $x/L$.

**Figure 3.6** The normalized electric field distribution as a function of dose per exposure.

**Figure 4.1**: A schematic for the cross-sectional structure of a multilayer X-ray image detector. Here $d''$ and $d'$ are the thicknesses of the top and bottom blocking layers, respectively.

**Figure 4.2** MTF($f$) for a positively biased and 830 μm thick $MAPbI_3$ X-ray detector at 100 kVp X-ray exposure. The applied electric field $F$ = 0.06 V/μm and the average photon energy is 52.4 keV.

# List of Tables

# List of Abbreviations

| | |
|---|---|
| A/D | Analog to Digital |
| AMA | Active Matrix Array |
| FPD | Flat-Panel Detector |
| AMFPI | Active Matrix Flat-Panel Imager |
| TFT | Thin Film Transistor |
| a-Si:H | Hydrogenated Amorphous Silicon |
| EHP | Electron-Hole Pair |
| $MAPbI_3$ | Methyl Ammonium Lead Iodide |
| $MAPbBr_3$ | Methyl Ammonium Lead Bromide |
| PGR | Photogenerated Ratio |
| CCE | Charge Collection Efficiency |
| ITO | Indium Tin Oxide |
| PEDOT: PSS | Poly Polystyrene Sulfonate |
| PCBM | Phenyl-$C_{61}$-butyric acid methyl ester |
| ZnO | Zinc Oxide |
| CB | Conduction Band |
| VB | Valence Band |
| Ag | Silver |
| MTF | Modulation Transfer Function |
| LSF | Line Spread Function |

# Chapter 1: Introduction

## 1.1 X-ray (an electromagnetic wave)

The discovery of X-rays in 1895 by Wilhelm Roentgen was the turning point for the medical diagnosis of internal organs. It can penetrate through most objects, including the human body. X-rays are electromagnetic waves that are energetic enough that when interacting with an atom can liberate orbital electrons [1]. X-rays are produced in an x-ray tube. Electrons are accelerated from the cathode filament of the x-ray tube and targeted towards a metal anode such as Tungsten, due to the application of a high voltage between the two ends of the x-ray tube, the electrons gain sufficient kinetic energy and bombard the metal and release energy in the form of heat and radiation. A vacuum chamber is employed to prevent ionization of air molecules and reduction of X-ray generation efficiency. A very small amount of released energy is used to knock an electron from the inner shell of the targeted metal. Hence, electrons from higher energy level tend to fill up the vacancy and emits X-ray photons. The unit of X-ray exposure is Roentgen (R) in CGS and it has a unit of Gray (Gy) in SI unit system. It is a measure of X-ray radiation, in terms of its ability to produce one positive and negative electrostatic charge in one cubic centimeter of air. [2]

## 1.2 X-ray Imaging

X-ray experiences different attenuation for different materials. This is the fundamental concept behind X-ray imaging in medical diagnosis. Depending upon the X-ray attenuation in the human body, it produces a gray image for tissue, a white image for bones, and dark black images for air respectively [3]. There are two types of X-ray imaging techniques widely used Analog X-ray Imaging and Digital X-ray Imaging.

### 1.2.1 Analog X-ray Imaging

An analog X-ray imaging technique produces images with the aid of photographic plates. These photographic plates tend to require special chemical treatments to facilitate the production of X-ray images in medical diagnosis. According to the process, patients need to be properly positioned in between the X-ray tube and photographic plate and subjected to X-ray exposure. After the exposure, the plates are removed for post-processing and image formation. The drawback of this technique is that it takes time to process the image and does not allow a further image correction.

### 1.2.2 Digital X-ray Imaging

In digital radiography, X-ray images can be visualized without the usage of any expensive and environmentally hazardous chemicals. Contrary to analog X-ray Imaging systems, the photographic plates are replaced by an X-ray detector that converts the X-ray to electrical signals. Then the analog signal is digitized with the aid of an analog to digital A/D converter. Digital X-ray allows prompt image formation with minimal delay through the usage of X-ray detectors, computers, and advanced image processing technology. The image quality is far superior to the conventional analog X-ray imaging systems. It allows instantaneous image formation thus X-ray images of patients can be sent to remote places for medical consultations.

### 1.2.3 Flat-Panel Detector (FPD)

The flat-panel detector is a digital sensor where X-ray penetrating through human body parts is incident on the sensor [4]. Flat-panel X-ray image detector essentially combines with Active-Matrix array (AMA) and it is called active matrix flat-panel imagers or AMFPI. The AMFPI consists of millions of pixels, each of which corresponds to the pixel of the image. Each pixel collects charge equivalent to the amount of radiation it receives. A pixel contains storage capacitor, TFT (thin-film transistor) and A/D converter. The TFT (thin-film transistor) acts as a switch to transfer the image information from the storage capacitor and the A/D converter facilitates the conversion from analog to digital signal. The AMFPI can readout an image within 1/30 seconds that makes them ideal for real-time X-ray imaging technique called fluoroscopy. It is the stored charge distribution on the capacitor of a pixel which forms the latent image. The stored charges are read out by scanning the pixel of each row by means of external electrical switches. Depending upon the process by which electron-hole pairs are generated there are two categories of detectors which includes Direct conversion detectors and Indirect conversion detectors.

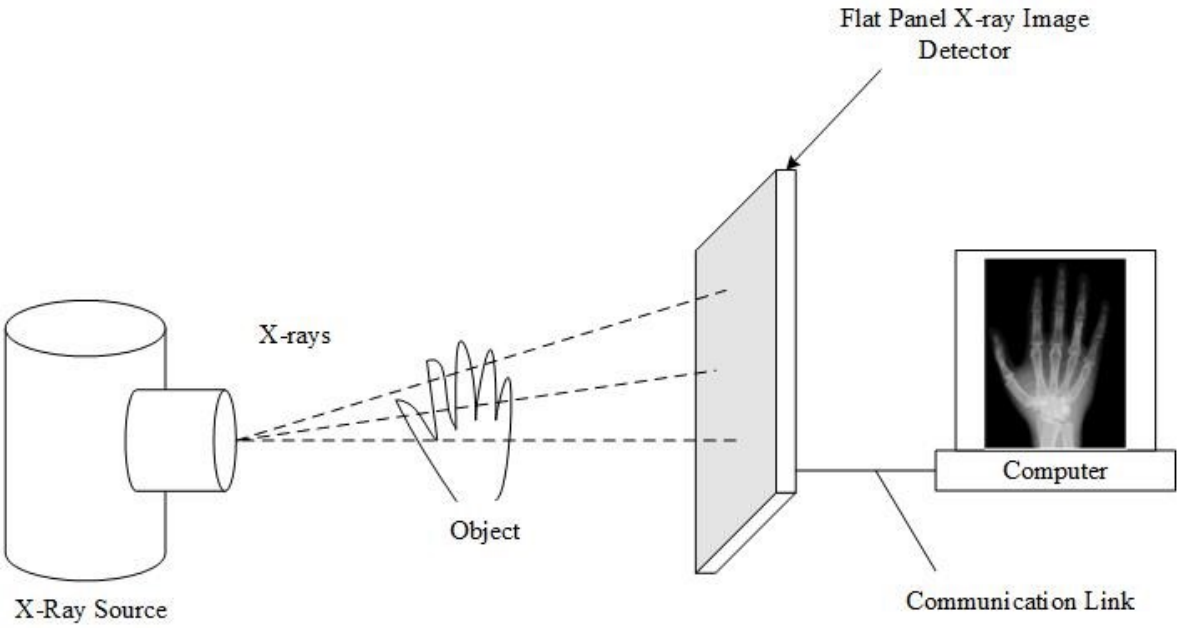


**Figure 1.1**: Schematic demonstration of a diagnostic image of patient hand with the aid of Flat Panel X-ray Image Detector.

### 1.2.4 Direct Conversion Detector

A simplified schematic diagram of a single pixel direct conversion X-ray detector is shown in figure-1.2. In a direct conversion X-ray detector, a suitable photoconductor directly converts the incident X-ray into charge. However, compared to an indirect approach, which is discussed later the conversion takes place without any intermediate stage. The electron-hole pairs are generated by the Photoelectric or Compton Scattering process immediately in the photoconductor after the X-rays are absorbed. Once the electron-hole pairs are generated, with the aid of suitable biasing the charges are ready to collect. The biasing of the electrode plays an important role in charge collection. The selection of polarity for biasing the electrode highly depends upon the charge transport properties (mobility and carrier-lifetime) which is an essential characteristic of a photoconductor. If the biasing is reversed, electrons will be collected at the storage capacitor. In figure-1.2, the photoconductor is positively biased, electrons tend to move towards the top electrode, holes are collected across the capacitor which is read by the thin-film transistors. A better resolution image quality is obtained with this scheme as X-rays do not experience any signal spreading to adjacent pixels, the electron-hole pairs are generated directly and multiple steps are

avoided, less additional noise is associated with direct X-ray conversion detectors. The fabrication process is simple since multiple layers are not required.

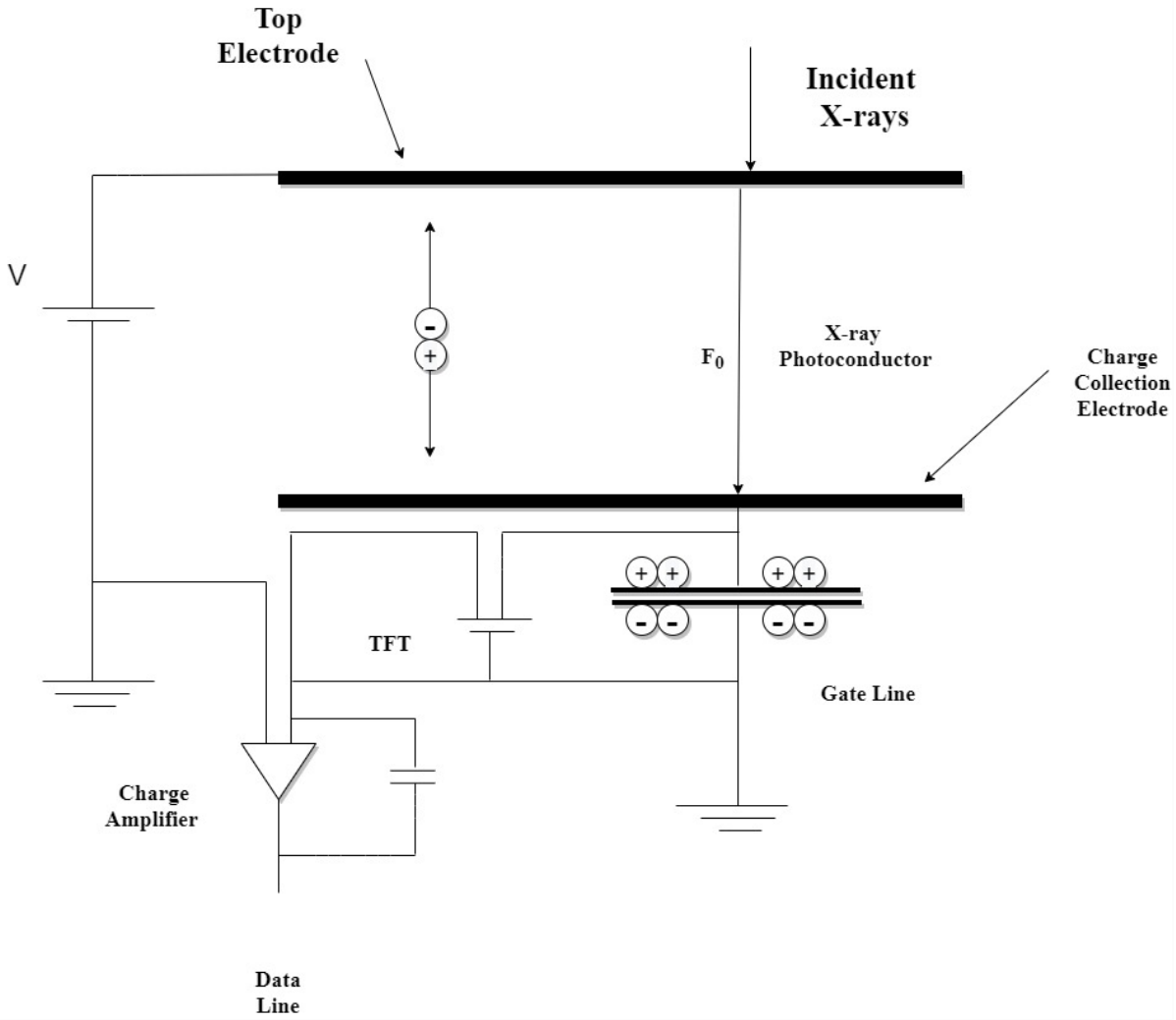


**Figure 1.2:** Simplified diagram of a single pixel direct conversion X-ray detector.

### 1.2.5 Indirect Conversion Detectors

Indirect conversion is another form of flat-panel detector which is used to generate charge from X-ray. The scintillator is the most important component for digital indirect X-ray converters as shown in Figure-1.3. When ionizing radiation such as X-ray interacts with a scintillator by Compton scattering or Photoelectric effect, electrons are excited to a higher energy state however, after some time the electron relaxes and falls back to the lower energy state resulting in the

production of photons in the frequency range of visible light. The scintillators are often mixed with a trace amount of activators such as thallium or sodium which creates energy states within the forbidden gap and allows electrons to relax from conduction band to activator energy states to the valence band as shown in figure-1.4. The scintillator converts X-ray into visible light which is detected by a P-I-N photodetector such as hydrogenated amorphous silicon (a-Si:H) and converts it to photogenerated charges. This process is inefficient as electrons in the scintillator emits lights corresponding to a frequency range of visible or ultraviolet light.

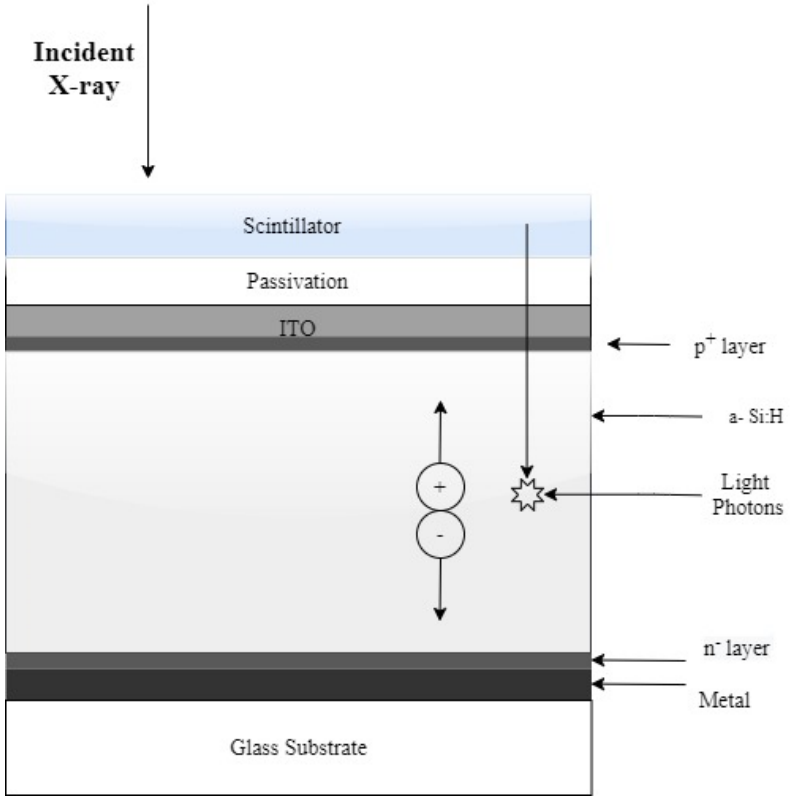


**Figure 1.3:** Simplified diagram of an indirect X-ray Detector (single pixel is shown in the diagram).

For indirect X-ray converters, CsI (Cesium Iodide) material is often used as scintillators. For medical purpose, it is not recommended to use the indirect X-ray converter as the resolution of images are poor and visible light generated often tend to spread to the adjacent pixels resulting in blurring of the images.

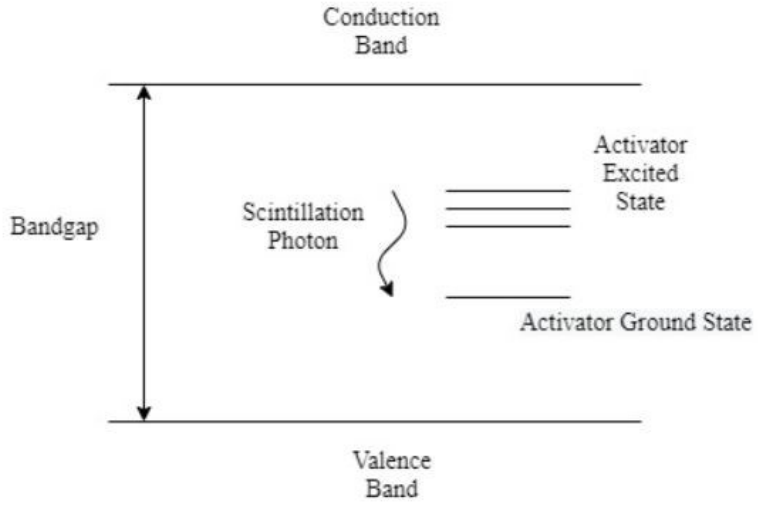


**Figure 1.4:** Simplified diagram illustrating the energy band of a scintillator.

### 1.3 Active-Matrix Readout Operation

In figure-1.5 shows a small, pixelated M×N (2480 × 3072) flat-panel AMA. Each pixel contains a storage capacitor and TFT which acts as a switch. The gates of all the TFTs in each individual row are connected to the same gate control line whereas all the TFTs in each column are connected to the same data line. If gate *i* is enabled, then TFTs corresponding to the *i* th row and all the columns starting from j =1 to N will be "turned on" and the charge will be transferred on the pixel electrodes in row M to the specific amplifier. Then the parallel signal is multiplexed from analog to digital signal form which is then transferred to the computer. The process is repeated for M+1 row until all the rows of AMA is readout.

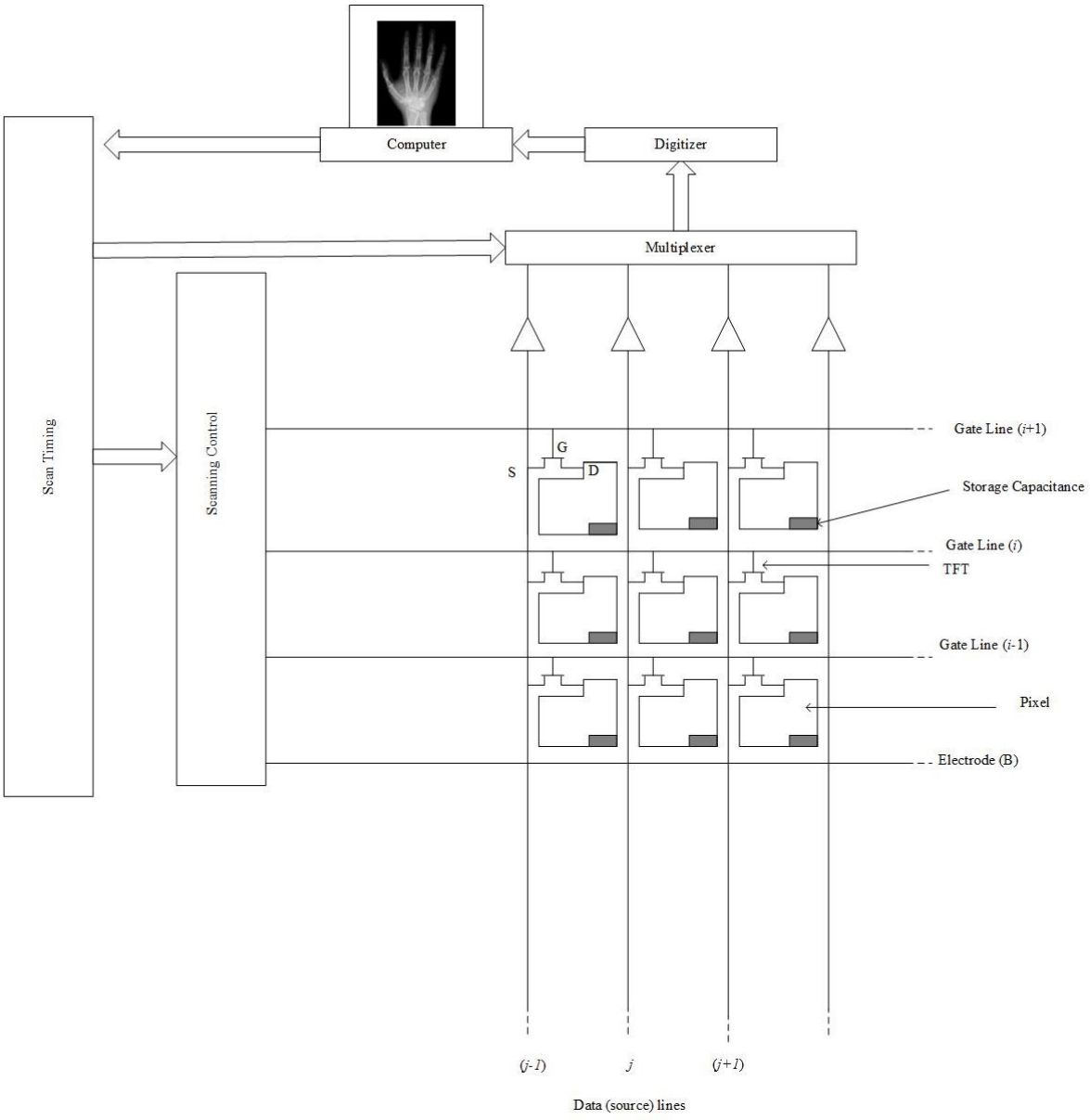


**Figure 1.5**: Schematic diagram illustrating a collection of pixels of Active Matrix Array (AMA) and electronics.

### 1.4 Ideal Photoconductors

The performance of direct conversion X-ray detectors relies upon the selection and design of the photoconductors. It is essential to compare the properties of a material with the concept of an ideal photoconductor for improved performance.

The properties of an ideal photoconductor should exhibit

a) To avoid unwanted patient exposure, most of the X-ray radiation should be absorbed within the photoconductor thickness. The absorption depth $\delta$ of X-ray should be significantly smaller than the photoconductor thickness $L$ ($\delta << L$).

b) The photoconductor must have high intrinsic sensitivity which means that it should be able to generate many collectable electron-hole pairs (EHP) for per unit exposure *i.e.*, the ionization energy $W$ of the photoconductor required to create one single electron-hole pair should be as small as possible. The ionization energy $W$ usually increases with the bandgap $E_g$ of the photoconductor [5].

c) There should be no bulk recombination of electrons and holes as the carrier drift towards the respective collection electrodes. Most of the electron-hole pairs are generated at the bulk. Usually, the recombination of carrier is negligibly small in medical diagnosis (exception at high exposure as this effect may prevail).

d) There should be negligible deep trapping of EHPs, that means that the schubweg $\mu\tau F' >> L$, where $\mu$ mobility of the carrier, $\tau$ is the deep trapping time and $F'$ is the applied electric field, $L$ is the photoconductor thickness. The schubweg is defined as the distance the carrier drifts before it is unavailable for conduction. In X-ray detectors, often image quality is deteriorated due to lagging and ghosting which relies upon the trapping rate.

e) The diffusion of carriers should be negligible compared to the drift. This property is important for better image resolution.

f) The dark current should be small as possible because it is unwanted noise. It arises mainly due to carrier injection from metal contact and thermal generation of the carrier in absence of any X-ray radiation. For a small dark current, a semiconductor material with a large bandgap is required which in turn reduces the concentration of photogenerated carriers as mentioned in (b). In clinical applications, the dark current of ~10 pA/cm$^2$ is acceptable.

g) The longest carrier transit time, carrier exhibiting smallest drift mobility, should be smaller than the actual read-out time.
h) The photoconductor properties should remain consistent i.e., the characteristics and properties should not be vulnerable to any change due to repeated exposure.
i) The photoconductor material should be able to conveniently be deposited throughout the AMA panel.
j) The photoconductor should maintain a uniform characteristic over its entire area.
k) Temporal artifacts such as *image lagging* and *ghosting* (discussed in detail in chapter 2) should be negligibly small.

## 1.5 Motivations

### 1.5.1 Present photoconduction utilization and its drawbacks

Modern X-ray imaging system is dominated by the usage of a-Se because its underlying features such as low dark current, convenient deposition over large area and suitable carrier transport properties. Compared to ideal photoconductor properties, a-Se fails in some circumstances. Although a-Se can produce superior quality X-ray images, it has low conversion gain. Low conversion gain is the inability of a photoconductor material to generate a large number of electron-hole pairs when X-ray radiation is illuminated. The ionization energy $W$ of a-Se is approximately 45 eV, so a huge amount of energy is required to produce one single electron-hole pair which leads to low conversion. The applied electric field should be large enough ~10V/μm for enough charge carrier generation, better charge collection, and image readout. The drift mobilities of a-Se is very low. The hole mobilities are ~ 0.12 $cm^2$/V-s and electron mobilities are ~0.003-0.006 $cm^2$/V-s [4]. Relatively poor charge carrier properties can lead to low image resolution and other temporal effects such as image lagging and ghosting which are discussed in chapter 2. One of the major drawbacks of a-Se which may limit its usage is poor sensitivity, due to high ionization energy. Many researchers are constantly trying to find a suitable candidate which can replace a-Se for X-ray detector systems. Recent publications [6, 7, 8] strongly indicate that organic perovskites can be a vital candidate to replace contemporary a-Se material in x-ray imaging detectors.

### 1.5.2 Merits and demerits of Perovskite material

Organic perovskite material provides low ionization energy compared to conventionally used a-Se. These materials can be efficiently and uniformly deposited with the aid of economically feasible solution-based chemical processes over a large area to design flat-panel detectors. Organic perovskite materials tend to have low ionization energy of approximately ~ 5 eV. The ionization energy is defined as the amount of energy supplied from incoming X-ray radiation to generate an electron-hole pair. One of the underlying features of this material is that it has excellent carrier transport properties, so it requires less applied electric field to drift the carriers which provide a better charge collection efficiency. As a result, organic perovskite has higher sensitivity than a-Se. However, there remain lots of scientific challenges such as obtaining a suitable detector structure that gives low dark current together with high x-ray sensitivity, image-resolution, signal-to-noise ratio, and long-term stability of material properties. Recent experiments [25] show that the x-ray sensitivity deteriorates under high accumulated doses. Moreover, the measured resolution in perovskite is much worse compared to a-Se detectors [8]. It is vital to investigate the underline the physical reasons for the above two phenomena in perovskite detectors by developing physics-based models, which will be very useful for optimizing the imaging performances of these detectors.

## 1.6 Research Objective

The main objective of this research is to conduct investigations to evaluate the physical interpretations of organic perovskite material in X-ray imaging detectors. The specific research objectives are:

- Development of a physics-based model to analyze the dynamic x-ray sensitivity.
- Investigate the sensitivity reduction mechanisms in organic perovskite material under repeated exposure.
- To propose an appropriate physics-based model to analyze the resolution in terms of modulation transfer function (MTF) for perovskite x-ray detectors.
- Investigate the loss of resolution mechanisms in organic perovskite detectors.

## 1.7 Organization of the thesis

In this chapter, the fundamental concepts of X-ray imaging and the process of image readout have been critically discussed. The thesis is comprised of four chapters. Eventually, the research objectives followed by research motivations will be discussed in the following chapters. In chapter 1, we discussed the X-ray imaging detectors followed by research objectives. The second chapter deals with important background theories, performance metrics of X-detectors, and characteristics of an ideal photoconductor. An investigation to evaluate the sensitivity reduction mechanism under repeated has been critically discussed in chapter 3. In chapter 4, the pre-sampling modulation transfer function of hybrid organic perovskite x-ray detector has been analyzed and discussed.

# Chapter-2 Background and theories

In this chapter, the properties of organic perovskite material and some of the important parameters that satisfy the requirement of an X-ray imaging detector has been discussed. In addition, some of the important fundamental concepts related to X-ray imaging detector has also been discussed.

## 2.1 Properties of Perovskite Material

The perovskite material was first discovered in 1836 by a German mineralogist Gustav Rose, the name perovskite was given in honor of a Russian mineralogist Lev Perovski [9]. The perovskite material has a crystal structure of calcium titanate ($CaTiO_3$) which is shown in figure-2.1. The chemical composition of organic perovskite is $ABX_3$ where A is organic monovalent cation $CH_3NH_3^+$ (methylammonium) or $NH_2CH_3NH_2^+$ (formamidine), $B^{2+}$ is a divalent cation usually $Pb^{2+}$ or $Sn^{2+}$ and $X^-$ is halide anion of $Cl^-$ or $Br^-$ or $I^-$. In figure-2.1, the organic monovalent cations $A^+$ are located in each of the eight corners of a unit cell, the divalent cation $B^{2+}$ is located at the center of the cube, and six $X^-$ halide anions are located octahedrally at each face of the unit cell respectively. The organic perovskite materials are relatively cheap and simple to manufacture which makes them a comparable candidate to silicon-based photovoltaics [10].

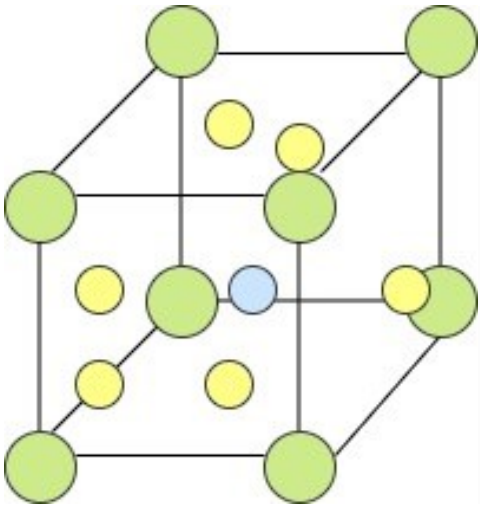

**Figure 2.1:** Shows the crystal structure of a single crystal of methylammonium lead iodide ($MAPbI_3$)

Organic perovskite can be prepared by one-step solution deposition or two-step solution deposition as shown in figure-2.2.

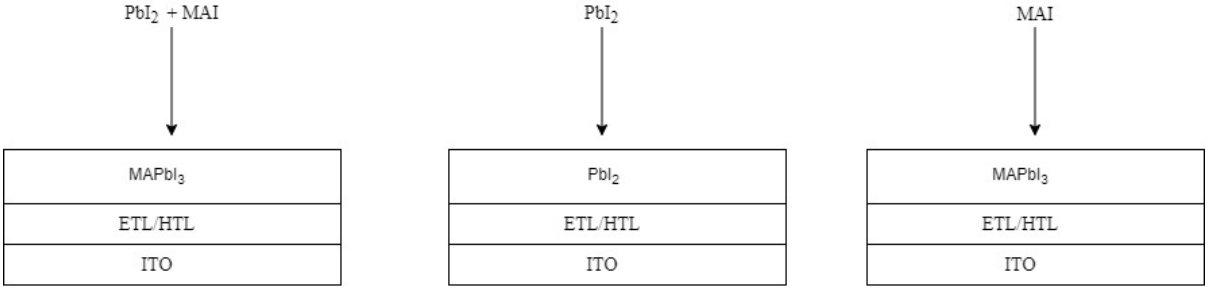


a) Single step solution deposition b) Two-step solution deposition

Figr-2.2 a) Shows single-step solution deposition solution process where Lead Iodide and Methyl Iodide have been simultaneously deposited to give the end product as desired Methylammonium lead iodide, this process is more efficient and rapid, but it is challenging to control the thickness of organic perovskite material. b) Shows two-step solution deposition process where Lead Iodide and Methylammonium iodide has been added in two-step separate steps, this process gives a more uniform film of organic perovskite [11].

### 2.2 Band gap Energy

The band gap $E_g$ is the energy difference between the top of the valence band and the bottom of the conduction band. It is defined as the minimum amount of energy required to excite an electron from the valence band to the conduction band. The carriers in the top of the valence band and bottom of the conduction band participate in the electronic processes. The band gap energy of complex three-dimensional Methylammonium lead Iodide ($MAPbI_3$) is obtained with the aid of density-functional theory and it is approximately ~1.6 eV. Table 2.2 shows the band gap of different halide perovskite materials.

| Perovskite Materials | Band gap ($E_g$) |
|---|---|
| $CH_3NH_3PbI_3$ | ~1.6 eV |
| $CH_3NH_3PbBr_3$ | ~2.34 eV |
| $CH_3NH_3PbCl_3$ | ~3.11 eV |

Table 2.2: Shows the approximate band gap of various organic perovskite materials. The band gap is a crucial parameter in optoelectronics research.

**2.3 Ionization Energy**

An atom is ionized when an electron is ejected due to the absorption of an incident X-ray photon, and it is usually denoted by $W_{\pm}$. In an atom, the ionization process can occur simultaneously by Photoelectric effect, Compton Scattering, and Rayleigh Scattering. The Photoelectric effect is the most dominating mechanism which results in the ionization of an atom. In Photoelectric effect interactions, all the supplied X-ray energy is absorbed by the medium, and it is transferred to the electron. A portion of this energy is used to overcome the binding energy of the electron, and the remaining fraction of the energy is converted to the kinetic energy of the ejected electron. At first, a single electron-hole pair (EHP) is generated. As the energetic primary electron moves with sufficient kinetic energy, it collides with other atoms along its path and causes further ionization. The probability of ionization due to secondary electrons is very small.

The ionization energy $W_{\pm}$ (or Electron hole pair creation) is defined as the minimum amount of radiation energy absorbed by a material to generate a single electron-hole pair. The collectable charge due to the absorption of incident radiation is given by $eE_{ab}/ W_{\pm}$, where $E_{ab}$ is the energy absorbed from the incident radiation, $W_{\pm}$ is the ionization energy, and $e$ is the elementary charge. The intrinsic sensitivity of a photoconductor relies upon the number of collectable free charges. Photoconductors having lower ionization energy generally tends to have higher sensitivity. For most cases, the $W_{\pm}$ is related to the band gap $E_g$ of the semiconductor and it is given by [12]

$$W_{\pm} \approx 2.8E_g + E_{phonon} \qquad (2.1)$$

where $E_g$ is the band gap of the semiconductor, $E_{phonon}$ is the phonon energy that arises due to the lattice vibration of atoms. In equation 2.1, $E_{phonon}$ is relatively very small thus ionization energy $W_{\pm}$ is almost equivalent to $2.8E_g$. Lower ionization is one of the important criteria which is relative to the ideal photoconductor, and it is discussed later in this chapter.

### 2.4 Charge Carrier Lifetime ($\tau$) and Mobility ($\mu$)

The charge carrier lifetime $\tau$ is defined as the average time carrier takes to recombine and becomes unavailable for conduction. The mobility $\mu$ is defined as the ability of the carrier to move through the material when an electric field is applied. The product of charge carrier lifetime and mobility ($\mu\tau$) is defined as charge carrier transport, and it is an important function to determine the sensitivity of a device.

The charge carrier lifetime and mobility depend upon deposition technique, nature of the film formed, and finally the detector structure. Considering these phenomena table-2.3 briefly describes the respective charge carrier lifetime ($\tau$) and mobility ($\mu$) of different organic perovskite with different halide compositions.

**Table 2.3** Shows the comparison of different organic perovskite compound with different crystal structure

| Perovskite Compound | Mobility ($cm^2$/V-s) | Charge Carrier lifetime ($\mu$s) |
|---|---|---|
| $CH_3NH_3PbI_3$ (Polycrystalline) | ~1-10 | ~0.01-1 |
| $CH_3NH_3PbI_3$ (Single crystal) | ~24-105 | ~0.5-1 |
| $CH_3NH_3PbBr_3$ (Polycrystalline) | ~30 | ~0.05-0.16 |
| $CH_3NH_3PbBr_3$ (Single crystal) | ~24-115 | ~0.3-1 |

## 2.5 X-ray Attenuation and Absorption

Attenuation is defined as the removal of incident X-ray photons from an X-ray beam by absorption or scattering events in a medium. Consider a beam of X-ray photons $N_l$ is irradiated perpendicularly on a thin plate having a thickness of *dl* as shown in figure- 2.3. The number of X-ray photons that interact with the medium is proportional to the product of the number of X-ray photons beams and thickness of the medium [2]. If $\alpha$ is the proportionality constant which is the probability of interaction, then the reduction of photons ($N_l$) from point of the incident is given by equation (2.2)

$$dN_l = -\alpha N_l dl \qquad (2.2)$$

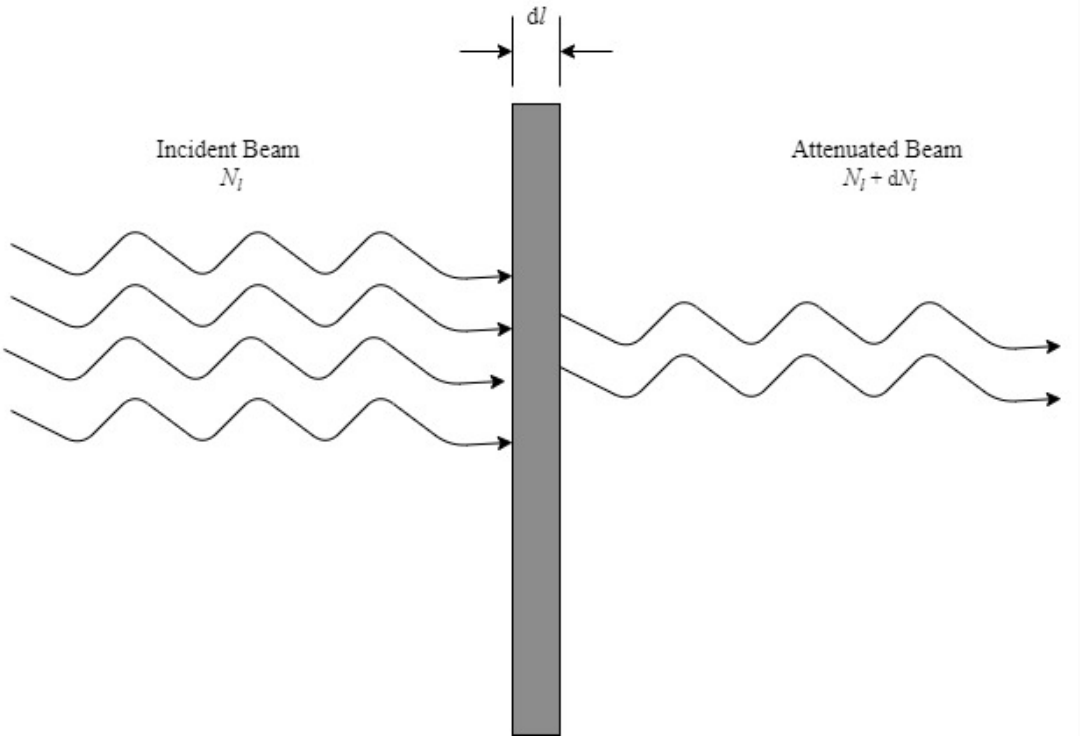


Figure 2.3: Demonstration of X-ray photon attenuation in a medium.

Rearrangement and integration of equation 2.2 gives,

$$\int_{N_i}^{N} \frac{dN_l}{N_l} = -\alpha \int_0^x dl, \qquad (2.3)$$

where $Ni$ is the number of incident X-ray photons and $N$ is the number of transmitted X-ray photons at a thickness of $x$ measured from the radiation receiving surface of the medium. Solution of equation 2.3 gives,

$$N(x) = N_i e^{-\alpha x} \tag{2.4}$$

From equation 2.4, the term $\alpha$ is referred to the linear attenuation coefficient of the medium. The linear attenuation coefficient is a material property, and it is different for different materials. The linear attenuation is a function of incident photon energy ($E_{ph}$), atomic number (Z), the density of the material ($\rho$). When an X-ray photon encounters a medium, a series of interactions occur in a random manner, but not all the incident X-ray photon energy is absorbed by the medium. A portion of the incident X-ray photon energy is radiated from the medium which is regarded as scattered radiation and the remaining part is converted into kinetic energy of a high-speed electron. After a series of interactions of incident photons with the medium, it is possible to determine the average absorbed energy per photon, which is given by $E_{ab}$, and the absorption coefficient as a function of energy is $\alpha_{en.}$ The relationship between energy absorption coefficient and linear attenuation is given by [10]

$$\alpha_{en} = \alpha \frac{E_{ab}}{E_{ph}} \tag{2.5}$$

From equation (2.4), the absorbed energy profile in the medium can be expressed as

$$E'_{ab}(x) = E_{ab}\alpha N_i e^{-\alpha x} \tag{2.6}$$

It is required to calculate the number of incident photons; $N_i$ is directly proportional to the photon fluence $\phi$ of the incident photon. The photon fluence is defined as the number of photons per unit area per unit Roentgen (R). If $X$ is the exposure measured in Roentgen (R), and $A$ is the area of the medium then the incident photon is given by,

$$N_i = A\phi X \tag{2.7}$$

Considering per unit exposure, the expression for photon fluence $\phi$ can be written as,

$$\phi = \frac{5.45\times10^{13}}{\left(\alpha_{en}/\rho\right)_{air} E_{ph}} \tag{2.8}$$

Where $E_{ph}$ is the incident photon energy considering monoenergetic beam, ($\alpha_{en}$)-air is the energy absorption coefficient of air, $\rho_{\text{air}}$ is the density of air. The parameter is called the mass-energy absorption coefficient of air, which is a function of photon energy $E_{ph}$. Substituting (2.8) in (2.7) and then finally to (2.6) gives,

$$E'_{ab}(x) = \frac{5.45\times10^{13}}{\left(\alpha_{en}/\rho\right)_{air} E_{ph}} AXE_{ab}\alpha e^{-\alpha x} \tag{2.9}$$

Using equation (2.5) in (2.9) gives,

$$E'_{ab}(x) = \frac{5.45\times10^{13}}{\left(\alpha_{en}/\rho\right)_{air}} AX\alpha_{en} e^{-\alpha x} \tag{2.10}$$

The fraction of X-ray photons that are attenuated in the medium is called quantum efficiency and is expressed by,

$$\eta = \int_0^L \frac{\alpha N_i e^{-\alpha x}}{N_i}\, dx \tag{2.11}$$

where $L$ is the thickness of the medium. Equation (2.11) gives $\eta = 1 - e^{-\alpha L}$ which states that the probability of the incident X-ray photon has been attenuated within the medium. The attenuation depth $\delta$, is the reciprocal of $\alpha$, where 63 percent of the incident X-ray photon has been attenuated. To reduce the patient dose, it requires most of the incident X-ray photons should be attenuated within the detector structure (i.e., the thickness of the detector $L$ should be much larger than $\delta$) and thus, it is preferable to use suitable photoconductor material with high absorption coefficient $\alpha$ (low $\delta$). Usually, the detector thickness $L$ should be much greater than attenuation depth $\delta$, but there is a trade-off between the thickness of the detector and charge collection efficiency as charge carriers travel a greater distance hence it increases the probability of trapping and recombination of carriers, thus carrier loss becomes more probable as they drift along the detector thickness to reach the electrodes.

## 2.6 X-Ray Sensitivity

The sensitivity of an X-ray image detector is defined as the collected charge per unit area per unit exposure of radiation,

$$S = \frac{Q}{AX} \qquad (2.12)$$

where $Q$ is the collected charge in Coulomb (C), $X$ is the incident radiation measured in Roentgen (R), and $A$ is the area of the photoconductor in ($cm^2$). The unit of sensitivity is $C/cm^2/R$. One Roentgen is defined as the amount of radiation required to create ions carrying a total charge of $2.58\times10^{-4}$ C per kg of air [13]. The average energy required to produce an ion pair is 33.97 eV or 33.97 J/C.

1 R = $2.58\times10^{-4}$ C/kg × 33.97 J/C = 0.00876 J/kg = 8.76 mGy.

A simplified circuit diagram of the X-ray detector is shown in Figure-2.4. A thick layer of the photoconductor is sandwiched between two parallel plates of electrodes. The top electrode is a radiation-receiving electrode, and the bottom electrode is a pixel electrode. The top electrode is biased with a voltage V, to establish an electric field $F_0$ (V/μm) in the photoconductor. The biasing can be positive or negative depending upon the photoconductor material. The absorption of incident X-ray radiation results in the generation of EHPs. The photogenerated carriers are drifted in opposite directions due to the applied electric field. The movement of photogenerated carriers results in transient photocurrent, integration of photocurrent gives collected charge. The charge gathers at the storage capacitor and TFT acts as a switch that is turned on to read the charge from the external circuit. The integration time is much longer than the X-ray exposure time.

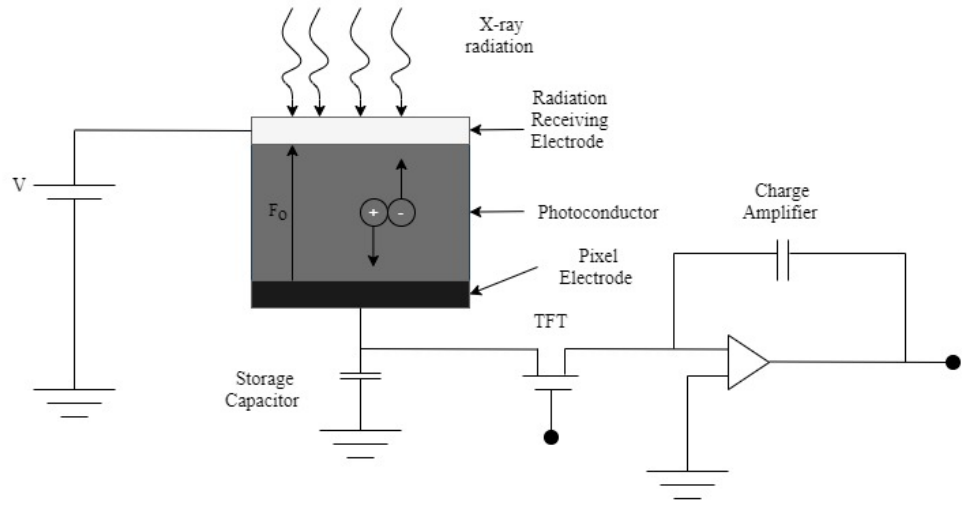


Figure 2.4: Schematic diagram demonstrating the circuit equivalent of an X-ray image detector.

The experimentally obtained sensitivity of organic perovskite X-ray image detectors are 25μC/mGy for $MAPbI_3$ polycrystalline films and 80μC/mGy for $MAPbBr_3$ single-crystal films. These experimental results suggest that the sensitivity of organic perovskite material is comparable to conventionally used a-Se-based X-ray image detectors.

The sensitivity of a photoconductor material is usually expressed in terms of normalized sensitivity. The normalized sensitivity, *Sn* is defined as the ratio of the actual sensitivity to the maximum sensitivity that would arise if all the incident photons were attenuated within the detector structure and all liberated charge carriers were collected by the electrodes. Hence, it is assumed that the quantum efficiency is unity. In section-2.3, it is mentioned that the total collectable charge generated due to absorption of incident photon energy, $E_{ph}$ is $eE_{ab}/ W_{\pm}$. Therefore, the maximum collectable charge is,

$$Q_o = \int_0^{\infty} \frac{eEab\prime}{W_{\pm}} dx \qquad (2.13)$$

In equation (2.13) it is assumed that the ionization energy $W_{\pm}$ is independent of an applied electric field. Substituting equation (2.9) into (2.13) gives,

$$Q_o = \frac{5.45\times10^{13}e}{W\pm\left(\alpha_{en}/\rho\right)_{air}} AX(\alpha_{en}/\alpha) \qquad (2.14)$$

The average electron and hole photocurrents are $i_e(t') = (ev_e/L)exp(-t/\tau_e')$ and

$i_h(t') = (ev_h/L)exp(-t/\tau_h')$, where $v_e = \mu_e F$ and $v_h = \mu_h F$ respectively, where $F$ is the applied electric field, $v_{e,h}$ are the drift velocities of holes and electrons, $\mu_{e,h}$ the mobilities of electrons and holes, $L$ is the photoconductor length, $\tau_{e,h}$ is the carrier lifetime, $e$ is the elementary charge of an electron.

$$Q' = \int_0^{t_e} i_e(t')dt' + \int_0^{t_h} i_h(t')dt' \quad (2.15)$$

$$Q' = x_e\left[1 - e^{-\frac{x'}{\mu_e \tau_e' F}}\right] + x_h\left[1 - e^{-\frac{(L-x')}{\mu_h \tau_h' F}}\right] \quad (2.16)$$

where $x_e = \frac{e\mu_e \tau_e' F}{L}$ and $x_h = \frac{e\mu_h \tau_h' F}{L}$ are the normalized schubweg which is defined as the distance traveled by the carrier before the carrier is unavailable for conduction. Equation 2.16 is the well-known ***Hect-Equation*** which is used to calculate the collected charge. If $Q'$ is the actual collected charge then the normalized sensitivity can be expressed as,

$$S_n = \frac{Q'}{Q_o} \quad (2.17)$$

In an actual case, the detector structure with finite photoconductor thickness, some of the incident photons will be transmitted i.e., the incident photons will not be attenuated within the photoconductor. Therefore, in actual detector X-ray generated charge within a finite thickness L is given by,

$$Q_g = \frac{5.45\times10^{13} e}{W\pm\left(\alpha_{en}/\rho\right)_{air}} AX(\alpha_{en}/\alpha)\eta \quad (2.18)$$

where $\eta = 1 - e^{-\alpha x}$ is the quantum efficiency of the photoconductor, Using equations (2.14) and (2.16) gives,

$$Sn = \frac{Q'}{Q_g}\eta \quad (2.19)$$

In some practical photoconductors, due to repeated exposures, the trapped charge carriers change the electric field profile and $W_{\pm}$, hence it changes the actual collected charge. Considering the effect of non-uniform electric on $W_{\pm}$. the normalized sensitivity can be expressed as,

$$S_n = \frac{Q_{actual}}{Q_g} \times \frac{Q'}{Q_{actual}}\eta \quad (2.20)$$

where the first term is referred to as photogenerated-ratio (***PGR***) and the second term is charge collection efficiency (***CCE***). In some practical photoconductors, charge collection efficiency is less than unity as photogenerated carriers are trapped.

### 2.7 Organic perovskite-based X-ray detector Structure

The experimentally proven X-ray detector structure using polycrystalline $MAPbI_3$ has been demonstrated in figure-2.6. A blocking layer (ZnO) is used to prevent unwanted carrier injection, but the device was susceptible to have an injection of carriers due to high biasing voltage ~ 7 V [6].

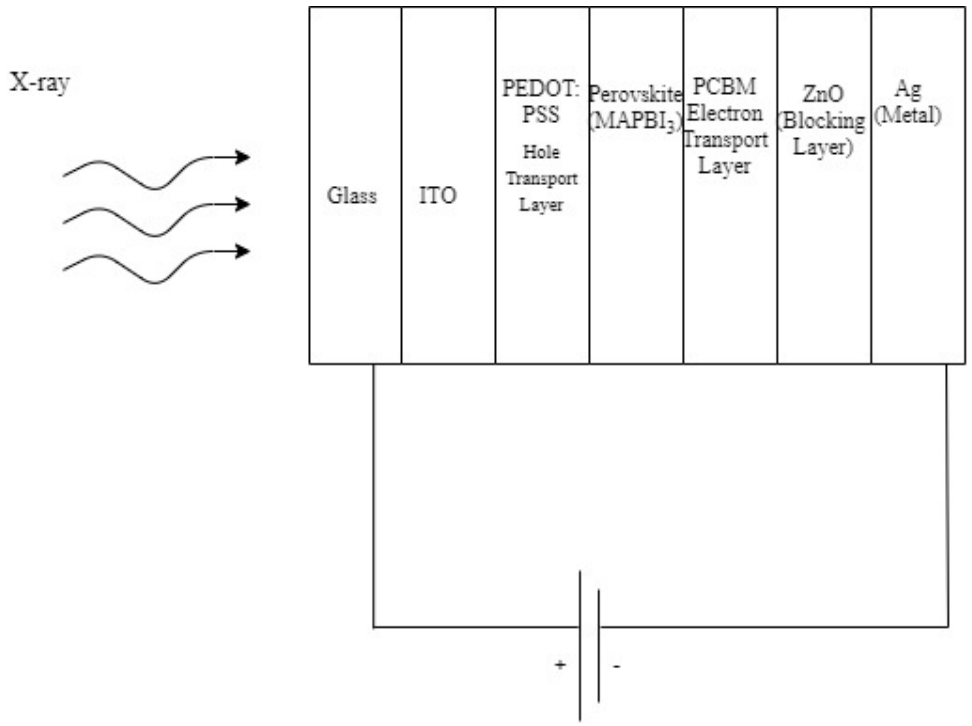


Figure 2.5: Demonstrating experimentally proven X-ray detector structure using polycrystalline $MAPbI_3$ perovskite material [6,7]. In figure-2.6, another experimentally proven X-ray detector structure has been demonstrated using single-crystalline Methylammonium Lead tribromide ($MAPbBr_3$). The active layer of this device is (~2 mm) and a low biasing voltage of (~0.1 V) has been applied which makes $MAPbBr_3$ based X-ray detector structure instrumental to avoid undesirable photo-gain [7].

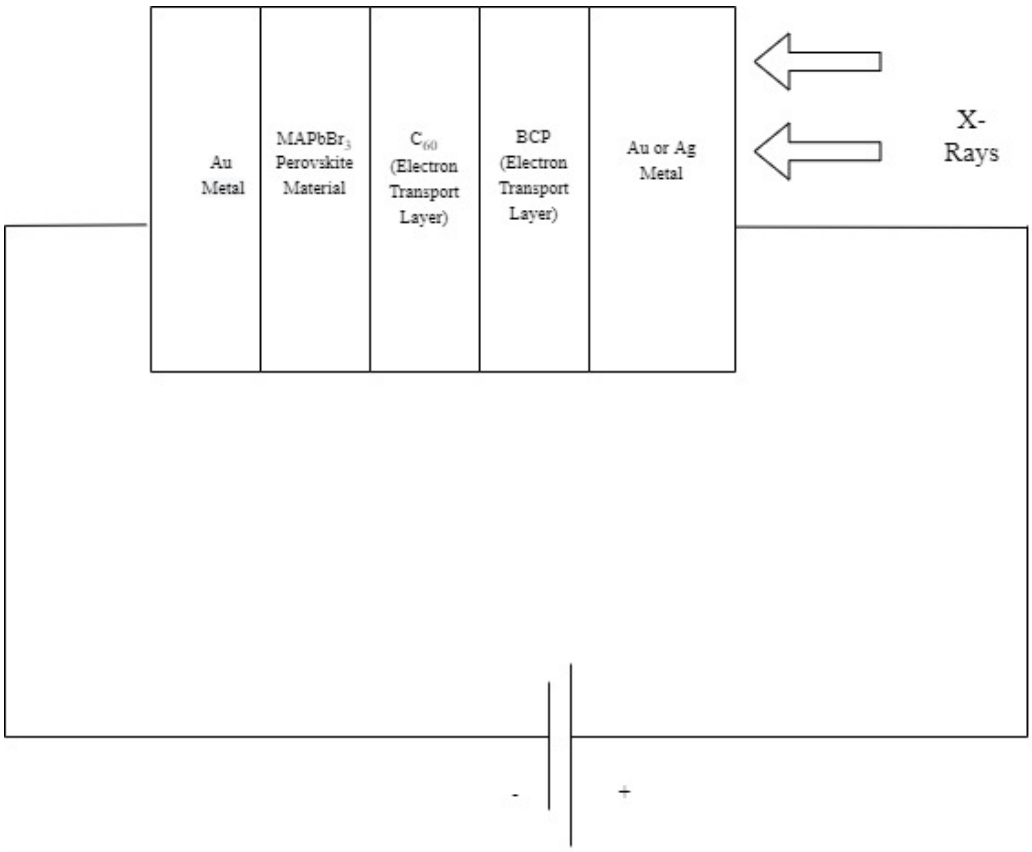


Figure 2.6: Shows the experimentally proven X-ray Image detector structure with Methylammonium Lead Tribromide ($MAPbBr_3$) [6].

**2.8 Recombination of Charge Carriers**

Recombination of electrons and holes is defined as the process by which photogenerated charge carriers annihilate each other resulting in loss of carriers. Primarily there are two types of recombination as radiative and non-radiative recombination. In the case of radiative recombination, electrons and holes recombine and thus generate photons. In the case of non-radiative recombination, the electron energy is converted to lattice vibration which is referred to as phonons. The reduction of sensitivity of a photoconductor material in excess repeated exposure occurs mainly due to trapping and recombination. Recombination results in loss of X-ray generated charge carriers. In figure-2.7 illustrates the fundamental concepts of recombination processes which primarily occur in semiconductors.

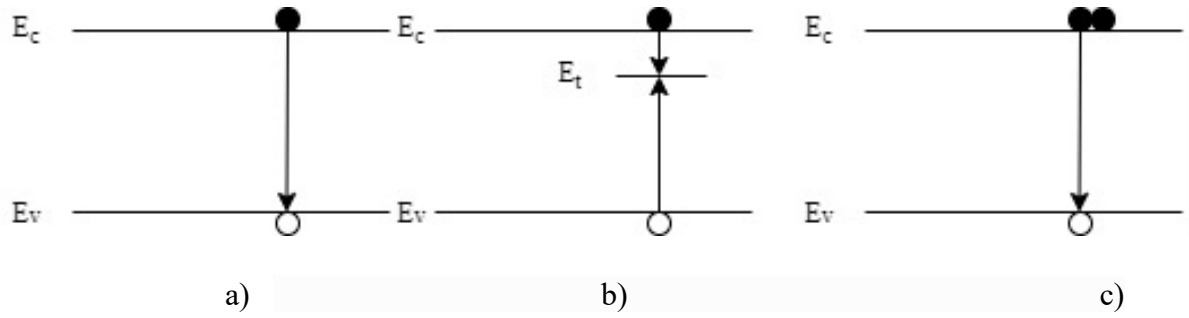


Figure 2.7: Demonstrates the recombination processes that occurs in semiconductors [14].

a) Bimolecular recombination in which electrons in the conduction band relaxes and recombines with a hole in the valence band, in direct semiconductor materials such recombination results in radioactive recombination b) Monomolecular or Trap-assisted recombination where trap energy band is present in the forbidden gap due to structural defect of the material, electrons are trapped with $E_t$ energy and encounters holes c) Auger recombination where there is band-to-band recombination, the recombination energy is used to generate a secondary electron and sometimes the excess energy is released as lattice vibration which is regarded as phonons. This process occurs under the high level of instantaneous free charge carriers in the materials. This recombination process is negligible in x-ray detectors because the instantaneous free charge carrier concentration is negligible is quite low in x-ray detectors.

### 2.9 Dark Current

The current that flows through the detector without irradiance of X-ray or light is termed as dark current. The dark current should be as small as possible because it is a source of noise [4]. There are three possible ways by which dark current is usually generated in an X-ray detector which includes depletion of carriers from defect states after biasing voltage, thermal generation of carriers in the bulk, and carrier injection from the metal contacts. The carrier injection from the metal contacts is the dominating mechanism that contributes to undesirable dark current, and it can be controlled by interfacing the metal/semiconductor region with suitable blocking layers with large bandgaps. The dark current is an unacceptable noise that adheres to signals, and it cannot be completely nullified from the detector. The acceptable range of dark current is between 2-100 $pA/cm^2$. The carriers are often trapped in the photoconductor due to the flow of dark current through the detector which is responsible for the modification of the internal electric field thus it affects the charge collection efficiency. Dark current is also responsible for image blur in an X-

ray imaging detector. The range of dark current in organic perovskite material is in the range of nano-amperes.

### 2.10 Modulation Transfer Function (*MTF*)

The modulation transfer function measures the efficiency of an imaging system such as an X-ray detector to resolve(transfer) different spatial frequencies of information in an image. It is also defined as the relative response of the system as a function of spatial frequencies. Consider an image containing a periodic black stripe with an interval of white space as shown in figure-2.8. As a result, each cycle forms a line pair with a bright stripe with its adjacent dark stripe. The distance between the bright stripe and its adjacent dark stripe is 1 mm as shown in image A figure-2.8. Thus, the spatial frequency becomes 1 line space per millimeter, 1 lp/mm respectively. In figure-2.8, the spatial frequencies for images B and C are 2 lp/mm and 4 lp/mm. The ability of the detector to resolve the spatial frequencies of the respective images is shown in figure-2.8. The detector can resolve 100 % for image A, efficiency has deteriorated slightly for image B, but the information is completely lost which represents 0 % transferring ability.

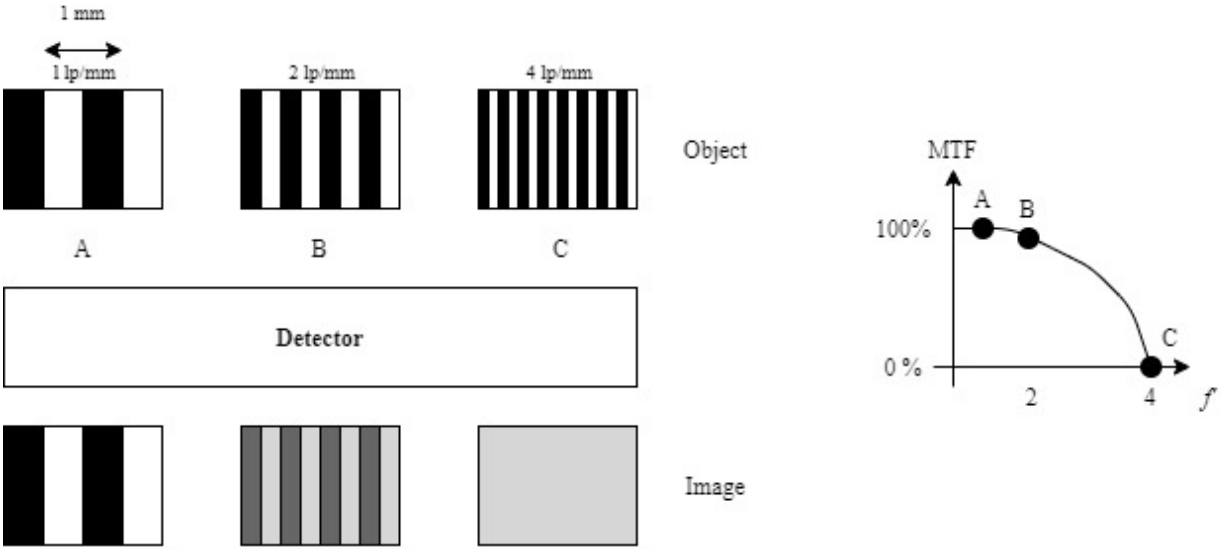


Figure 2.8: It illustrates the Modulation transfer function which is an important parameter to evaluate a detector performance. It measures the efficiency of the X-ray detector to resolve spatial frequencies of information in an image. The detector can resolve 100% for image A, the efficiency has reduced slights for image B, and the detector failed to resolve (transfer) information for image C.

Resolution or resolving power is defined as the ability to record separate small images placed in proximity to each other. The spatial resolution of a detector is described in terms of MTF. The X-ray imaging system contains several individual stages, thus the MTF of an imaging system is described as the cascade of individual stages but the overall MTF also referred to as presampling MTF is simply the product of MTF. The overall *MTF(f')* is a function of spatial frequency which is relatively described as the product rather than convolution. In general, a one-dimensional technique called the Line spread function (LSF) is more often used to describe the MTF of an X-ray imaging system. The Fourier transform of one-dimensional LSF provides the equivalent MTF of an X-ray imaging system. In figure-2.9, shows the response of a system to a line delta function. The overall MTF (presampling MTF) is the product of individual MTFs can be expressed as,

$$MTF(f') = MTF_m(f') \times MTF_a(f') \quad (2.21)$$

where $MTF_m(f')$ is the modulation transfer function of the detector of the material, $MTF_a(f')$ is the modulation transfer function associated with the aperture function of the pixel electrode. $MTF_a(f')$ arises due to averaging the signal over the pixel electrode. The aperture function defines the spatial frequencies of information is passed over the detector element.

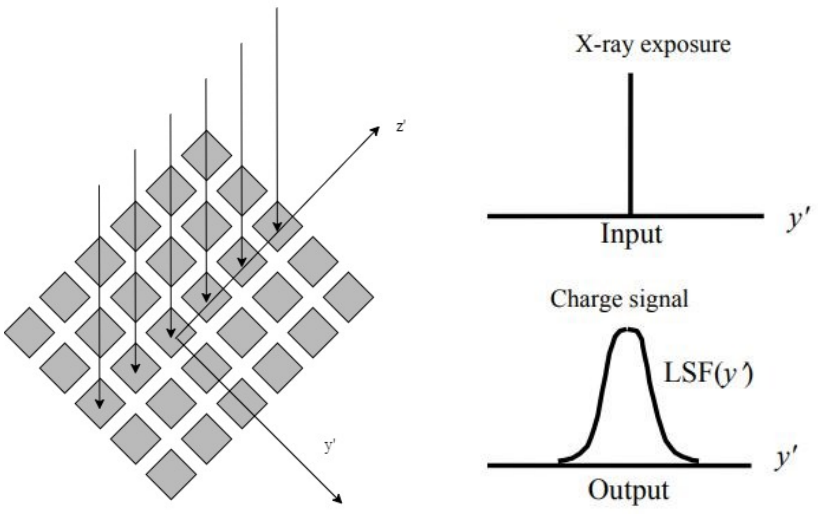


Figure 2.9: It demonstrates X-rays are incident along the line (along *z'* in the figure) over the pixel electrodes of the image detector, where the *y'z'* forms a plane of the image detector. The X-rays

incident upon the *y'* represents the delta function. The output charge signal along the line *y'* is spread out presents the LSF*(y'*).

In figure-2.10, the *geometric* pixel aperture width in a flat panel detector is smaller than the pixel pitch. The pixel pitch is the distance between the center of one pixel to the adjacent pixel. If the aperture is a square dimension with a width of *a'*, it is often represented as sinc(*a'f'*) function.

The *sinc* function is expressed as

$$MTF_a(f') = |sinc(a'f')| = |\frac{\sin(\pi a' f')}{\pi a' f'}| \qquad (2.22)$$

$MTF_a(f')$ as a function of spatial frequency is shown in figure 2.10b. The $MTF_a(f')$ becomes zero at spatial frequencies of $1/a'$ and $2/a'$

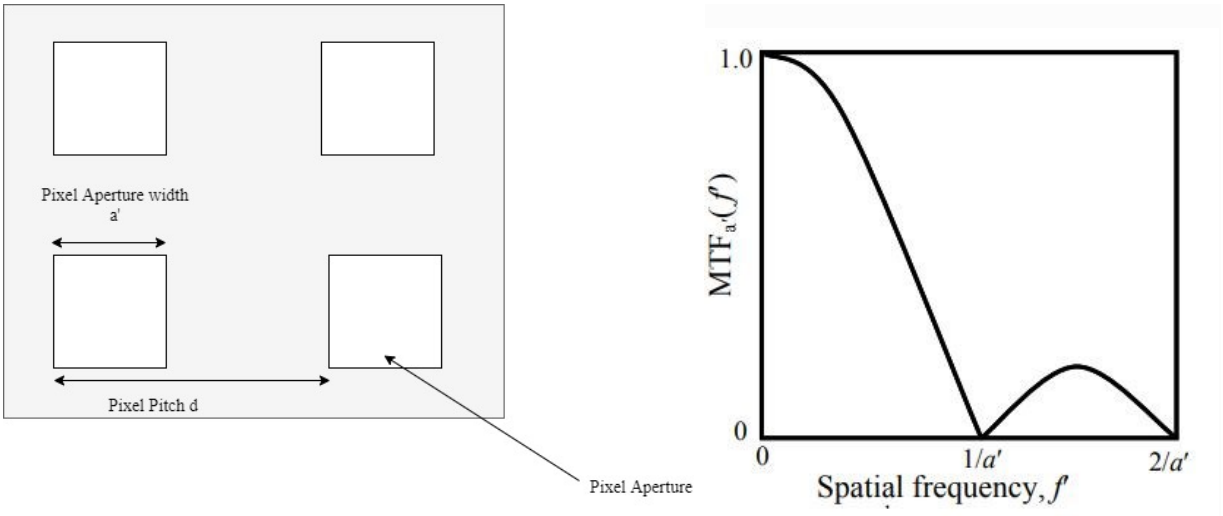


a) b)

Figure 2.10: a) Pixel aperture width and pixel pitch. b) $MTF_a(f')$ as a function spatial frequency *f'*.

The first zero of MTF(*f'*) occurs at $1/a'$.

The spacing between the pixel pitch determines the highest frequency (*Nyquist frequency,* $f_{ny}$) that can be imaged in an X-ray imaging system. The spacing between the samples is *d*, the Nyquist frequency is $1/2d$, the aliasing takes place takes place between $1/2d$ and$1/a$.

### 2.11 Image Lag and ghosting

The X-ray imaging systems should be designed in such a way that there should be negligible image lag or ghosting. When X-rays are incident upon photoconductors, charge carriers are created due to Photoelectric and Compton Scattering. The charge carriers tend to move due to biasing voltage across the electrodes and thus a transient current flow through the photoconductor that reaches a steady-state value after the carrier transit time [15]. For an ideal case, there should be photocurrent only when the detector is subjected to X-ray exposure and drop to zero abruptly after the radiation is removed. In practical photoconductors, there are defect states or trap centers that facilitate the trapping of carriers, the drifting carriers often trapped in the trap centers and releases later. The detrapping time depends upon their energy depth from the bandgap/mobility edges [16]. Due to the release of trapped carriers in photoconductor, after several seconds there is generation of unwanted transient current in absence of any X-ray exposure. It degrades the image quality as current of previous exposure combines the next one, generates X-ray image with inferior accuracy. Figure-2.11 (a) demonstrates image lag in an X-ray system.

Ghosting is defined as the change of X-ray sensitivity due to previous exposure to radiation. In presence of ghosting, a shadow of an impression of previous exposure is obtained due to subsequent exposure to radiation as shown in figure-2.11 (b). Ghosting is generally seen because of the reduction of sensitivity in particular regions subjected to previously exposed and can only be seen in subsequent X-ray images. In fluoroscopy where fast real-time X-ray images are taken, ghosting can affect the efficiency and accuracy of the diagnostic X-ray images

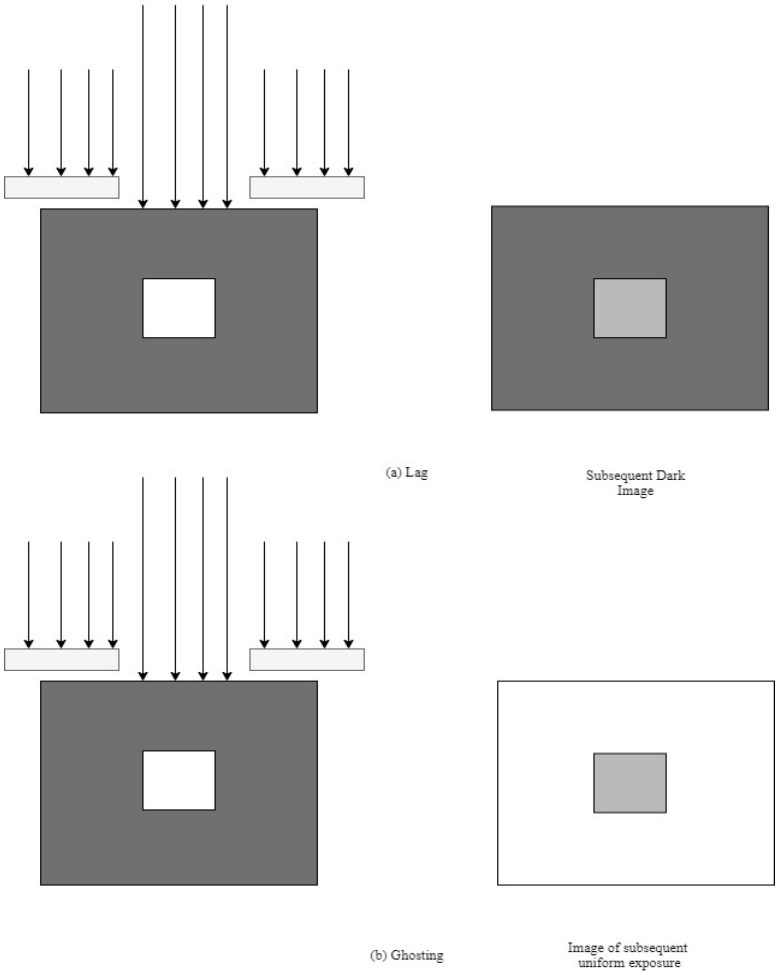


Figure-2.11: Demonstrates the characteristics of Image lag and ghosting taking place immediately after the exposure over a rectangular area. a) A dark image is obtained immediately after the X-ray exposure; Image lag is seen due to the interference of the X-ray image of previous exposure. b) A shadow of impression is acquired image is visible in subsequent uniform exposure. Ghosting arises due to the reduction of pixel sensitivity in particular areas subjected to subsequent uniform exposure.

# Chapter 3: Sensitivity reduction mechanism in organic perovskite X-ray detectors

The sensitivity reduction mechanisms in organic perovskite material have been critically analyzed, which has already been published [17].

The sensitivity reduction mechanisms in organic perovskite X-ray detectors are investigated in this paper by considering the dynamics of charge carrier transport across the perovskite photoconductor. A numerical model is proposed by considering bimolecular recombination, space charge effects, and charge carrier trapping (monomolecular) and detrapping. The coupled continuity equations for both holes and electrons, trapping rate equations, and the Poisson's equation across the photoconductor are simultaneously solved by a finite difference method. The numerical results are compared with COMSOL simulation. The change of sensitivity is not significant for a usual single exposure in diagnostic medical X-ray imaging applications. However, the sensitivity starts decreasing rapidly for an order of magnitude higher dose rate or accumulated dose under repeated exposures. The rapid change of electric field distribution (i.e., non uniform electric field) is mainly responsible for the reduction of X-ray sensitivity in perovskite X-ray detectors.

## 3.1 Introduction

Non-invasive medical imaging relies upon X-ray penetration through the body. To reduce medical complications on patients due to medical diagnosis, it is required a minimal X-ray dose deposition upon patients. Convenient deposition over a large area, moderate sensitivity, better resolution of images, and low dark current makes amorphous selenium (a-Se)-based X-ray imaging system a better choice for digital mammography [18]. However, the diagnostic applications of a-Se-based detectors get limited because of its high ionization energy (i.e., electron–hole pair creation energy), high voltage requirement, and relatively poor charge transport properties. Recently, polycrystalline organic perovskite ($MAPbI_3$) has been tested for the large area diagnostic medical imaging [19, 20]. Interestingly $MAPbI_3$ showed very good X-ray fluence ( $1.4 \times 10^7$ photons/mm$^2$ /s) with a convenient deposition (~100 μm) over a large area but a very high dark current. Later, Kim et al. [20]. proposed an innovative multilayer structure using blocking layers to reduce the dark current. Their structure showed reasonably low dark current, good X-ray sensitivity but very poor resolution in terms of the modulation transfer function. They also showed that the sensitivity does

not change up to a cumulative dose of 0.5 mGy. However, Shrestha et al. [21] showed that the X-ray in $MAPbI_3$ detector deteriorates at a higher dose rate. The change of sensitivity leads to the phenomenon called ‘‘ghosting’’ in X-ray imaging [22]. It is vital to investigate the physical origin of this change of sensitivity for the reliability of the detector. The mean X-ray exposures are 0.3 and 12 mR (1 R = 8.76 mGy) for diagnostic digital chest radiography and mammography [23]. In these dose rates, the X-ray generated free carrier concentration in a-Se detectors is quite low, and therefore, the effects of non-uniform electric field and bimolecular recombination are neglected in previous publications [22, 25]. Since the electron–hole pair (EHP) creation energy in $MAPbI_3$is almost an order of magnitude smaller than that in a-Se, the free carrier concentration in $MAPbI_3$ is an order of magnitude larger [22, 26]. Therefore, the effects of non-uniform electric field and bimolecular recombination in $MAPbI_3$ detectors may not be negligible. In this paper, we examine the mechanisms of change of X-ray sensitivity in polycrystalline $MAPbI_3$ detector by developing a numerical model. We simultaneously solve coupled Poisson, carrier continuity, and trapping rate equations for both electrons and holes in the photoconductor layer considering both monomolecular and bimolecular recombination. We also determine the range of exposure for which the small-signal model is valid by comparing the theoretical results with published experimental data [20, 21]. We examine the effects of non-uniform electric field and bimolecular recombination on the X-ray sensitivity of the $MAPbI_3$ detectors.

### 3.2 Numerical Model

In X-ray detectors, a photoconductor is sandwiched between two large-area parallel-plate electrodes and biased with a voltage V to the radiation-receiving electrode (top electrode) to establish an electric field in the photoconductor. The charge is collected from the bottom electrode. Most of the detectors use thin blocking layers between the bulk photoconductor and the electrode [20]. However, the thickness of these blocking layers is few microns, whereas the thickness of the bulk photoconductor layer is few hundred microns. For simplicity, we can assume that the incident X-rays are absorbed in the bulk, generate electron–hole pairs, and contribute to the photocurrent. We assume that the thermal equilibrium carrier concentrations are negligibly small, and that the dark current is negligible compared to the X-ray photocurrent. The diffusion of carriers is negligible compared with their drift because of the high applied field across the photoconductor [26] and the carrier transport is essentially one-dimensional. We assign a constant drift mobility and a single deep trapping time (lifetime) to each type of carrier (holes and electrons). Defining p

(x, t) as the free hole concentration, n (x, t) as the free electron concentration, $p_t$ (x, t) as the trapped hole concentration, and $n_t$ (x, t) as the trapped electron concentration at a distance x from the radiation-receiving electrode at time t, the continuity equations at positive bias for electrons and holes are

$$\frac{\partial n}{\partial t} = \mu_e \frac{\partial}{\partial x}(nF) - \frac{n}{\tau_e} - C_r pn - C_e p_t n + \frac{n_t}{\tau_{re}} + g_0 e^{-\alpha x} \quad (3.1)$$

$$\frac{\partial p}{\partial t} = -\mu_h \frac{\partial}{\partial x}(pF) - \frac{p}{\tau_h} - C_r pn - C_h p n_t + \frac{p_t}{\tau_{rh}} + g_0 e^{-\alpha x} \quad (3.2)$$

$g_0$ is the EHP generation rate at x = 0, $\alpha$ is the linear attenuation coefficient of the photoconductor, F is the electric field, L is the photoconductor thickness, $\mu$ is the drift mobility of charge carrier, $\tau$ is the deep trapping time of charge carrier, $C_r$ is the bimolecular recombination coefficient between free holes and electrons, and $C_{h\,(e)}$ is the capture coefficient between free hole (electron) and trapped electron (hole). The subscripts e and h represent electrons and holes, respectively. Perovskite $MAPbI_3$ is a direct bandgap semiconductor having bandgap energy of 1.6 eV and the trapping states are close to the band edges [27]. There are shallow traps at ~ 0.2 eV from the band edges and a deep trap of ~0.5–0.7 eV in the bandgap in poly-$MAPbI_3$ films [28]. Therefore, it is expected that the trapped charges be released relatively quickly since they are not very deep in the band. For modeling purpose, a characteristic release time $\tau_r$ is considered, which is a fitting parameter. The bimolecular recombination coefficients in low mobility semiconductors can be determined using Langevin model [29]

$C_r = C_L = e(\mu_h + \mu_e)/e$ and $C_{h,e} = e\,\mu_{e,h} / \varepsilon$, where $C_L$ is the Langevin recombination coefficient, e is the elementary charge, and $\varepsilon$ ( $= \varepsilon_0 \varepsilon_r$ , where $\varepsilon_0$ is the permittivity of free space and $\varepsilon_r$ is the static dielectric constant is the permittivity of the photoconductor. The bimolecular recombination coefficient in perovskite materials is few orders of magnitude smaller than that is predicted by the Langevin model [30]. The recombination coefficients are considered as fitting parameters in this paper. An exponentially decaying carrier generation rate is considered since the rate of generation follows the X-ray absorption profile across the photoconductor thickness. The expression of $g_0$ (in $cm^3\ s^{-1}$) is given by

$$g_0 = \frac{\phi_0 E \alpha}{T_{ex} W}, \quad (3.3)$$

where E is the X-ray photon energy in eV, W is the EHP creation energy in eV, α is in $cm^{-1}$, and $T_{ex}$ is the exposure time in seconds. The incident photon fluence (photons/$cm^2$) is [29]

$$\phi_0 = \frac{5.45\times10^{13} X}{(\alpha_{air} / \rho_{air}) E} \tag{3.4}$$

where $X$ is the X-ray exposure in roentgens, $\alpha_{air}$ and $\rho_{air}$ are the energy absorption coefficient and the density of air respectively ($\alpha_{air} / \rho_{air}$ is in $cm^2\ g^{-1}$). The amount of the trapped electron and hole concentrations can be calculated through the solution of trapping rate equation expressed as,

$$\frac{\partial n_t}{\partial t} = -C_h p n_t + \frac{n}{\tau_e} - \frac{n_t}{\tau_{re}} \tag{3.5}$$

$$\frac{\partial p_t}{\partial t} = -C_e p_t n + \frac{p}{\tau_h} - \frac{p_t}{\tau_{rh}} \tag{3.6}$$

The instantaneous electric field $F$ ($x$, $t$) due to the charge transport along the thickness of the photoconductor is calculated through the dynamic solution of Poisson's equations as,

$$-\frac{\partial^2 \Phi}{\partial x^2} = \frac{e}{\varepsilon}(p + p_t - n - n_t) \tag{3.7}$$

The electric field is derived from the potential as, $F = -\frac{d\Phi}{dx}$. The five coupled partial differential equations (1), (2), (5)–(7) are simultaneously solved by the finite difference method. The detail description of our finite difference technique was given in our previous publication [20]. The necessary initial conditions before any exposure are

$$p(x,0) = 0, \quad n(x,0) = 0, \quad p_t(x,0) = 0, \quad n_t(x,0) = 0, \quad \text{and } F(x,0) = V / L = F_0 \tag{3.8}$$

The boundary condition for electric field at any time is given by

$$\int_0^L F(x,t)dx = V \tag{3.9}$$

The photogenerated holes drift towards the bottom electrode and electrons move towards the top electrode due to the positive applied bias voltage. As holes drift to the bottom electrode immediately after generation, there will not be any hole present at the infinitesimal distance at $x$ =

0, which implies that the boundary condition is $p(0, t) = 0$. Similarly, the boundary condition for electrons, $n(L, t) = 0$.

The photocurrent density is given by

$$J(t) = \frac{e}{L}\int_0^L \left(\mu_h p + \mu_e n\right) F dx \tag{3.10}$$

Assuming that the exposure time is much longer than the carrier transit time, the collected charge ($C/cm^2$),

$$Q_c = \int_0^{T_{ex}} J\left(t\right) dt \tag{3.11}$$

Sensitivity, $S$ (charge collected per unit area per unit exposure) can be calculated as,

$$S = \frac{Q_c}{X} \tag{3.12}$$

**3.3 Results and discussions**

The numerical model is applied to $MAPbI_3$ X-ray detectors under various operating conditions. Some of the numerical model results are compared with the COMSOL simulation. The release of trapped carriers is considered when the exposure is off between successive exposures. The fraction of remaining trapped charge after the off-time $t_{off}$ can be calculated by solving equations (3.5) and (3.6), which is equal to $\exp(-t_{off}/\tau_r)$.

The dielectric constant and EHP creation energy in $MAPbI_3$ are 28 and 4.5 eV [7, 19]. Figure 3.1 shows the relative X-ray sensitivity of 830 μm thick $MAPbI_3$ X-ray detector as a function of accumulated X-ray dose at 100 kVp X-ray irradiation. This detector is suitable for chest radiographic applications, where the mean and maximum doses per exposure are 0.00263 and 0.0263 mGy, respectively. The average photon energy, $E_{av}$ = 52.4 keV, and an applied electric field $F_0$ = 0.06 V/μm. The dose rate and exposure time per pulse are 1 $mGys^{-1}$ and 50 ms, respectively. The dose per exposure is 0.05 mGy, which is almost double of the maximum exposure for chest radiography. The electron and hole mobilities are ~66 and 139 $cm^2/V/s$, respectively, according to the mentioned values in this article [20]. Note that the carrier mobility in polycrystalline perovskites is usually an order of magnitude lower than the mentioned values

above [29]. The experimental data were extracted from Extended Data Figure 4 of Ref. [20]. The model agrees well with the experimental data. The fitted values of deep trapping and release times for both electrons and holes are 20 μs (this value is within the range as mentioned in the Extended Data Figure 2 Ref [6]) and 30 ms, respectively. The transit time for the slower carrier (electron) is 2 μs. Since the release time is almost 4 orders of magnitude larger than the carrier transit time, the probability of carrier detrapping during carrier transit time is negligibly small. For the thermal release event, the release time $\tau_r = \nu^{-1}\exp(E_r/k_bT)$, where the $E_r$ is the trap-depth from the band edge, $k_b$ is the Boltzmann constant, $T$ is the absolute temperature, and $\nu$ is the attempt-to-escape frequency. Considering $\nu = 10^{12}$ per sec, the value of $E_r$ at room temperature becomes 0.62 eV, which is within the range of 0.5 – 0.7 eV as mentioned previously [28]. The fitted values of recombination coefficient, $C_r = 6.7 \times 10^{-9}$ cm$^3$ s$^{-1}$ and $C_h = C_e = 3.35 \times 10^{-9}$ cm$^3$ s$^{-1}$ which are almost 3 orders of magnitude lower than that predicted by the Langevin model. These fitted values of recombination coefficients and release time ($\tau_r$) remain the same in all calculations in this paper. The calculated value of X-ray photocurrent density is 0.0053 mAcm$^{-2}$, which is almost the same as mentioned in Figure 4 of Ref. [20]. The sensitivity reduction is negligible for this exposure range. This result indicates that the change of sensitivity at the exposure level close to the doses of diagnostic medical imaging is not significant.

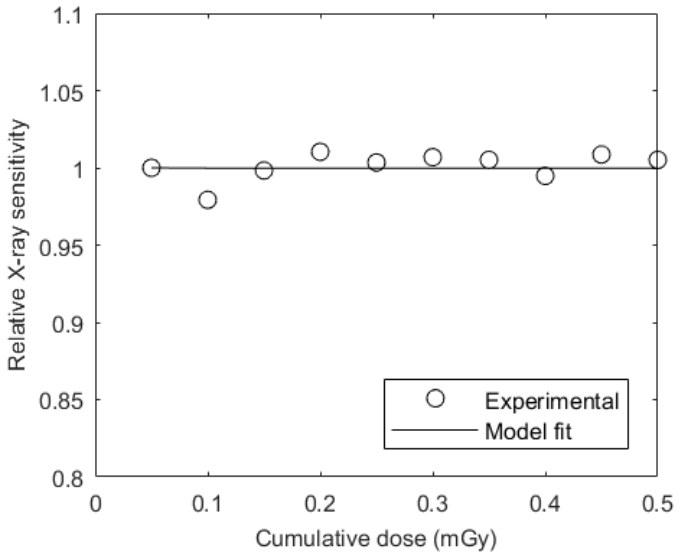


**Figure 3.1:** Relative X-ray sensitivity versus accumulated dose.

The concentration distributions of steady-state free and trapped carriers at the end of cumulative exposure of 0.5 mGy across the photoconductor layer are shown in Figure 3.2 (normalized distance = $x/L$). The steady-state free carrier concentrations are much smaller than the trapped carrier concentrations. The normalized electric fields ($F/F_0$) across the photoconductor layer at the end of the accumulated exposures of 0.025 and 0.5 mGy are shown in Figure 3.3. The electric field near the contacts increases by the expense of lowering electric field in the middle portion of the detector.

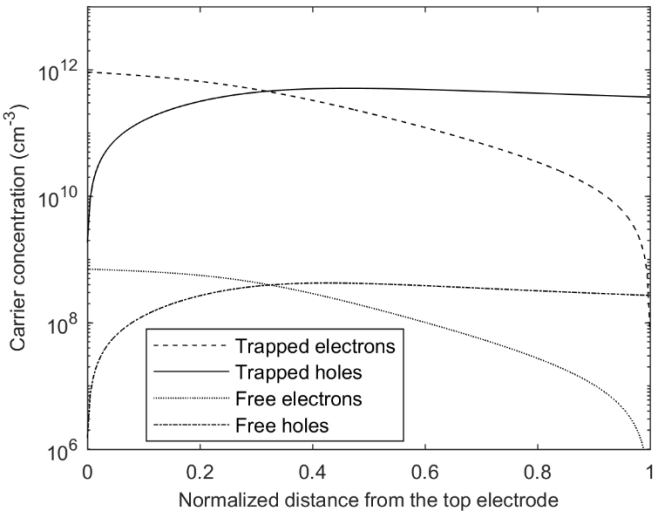


**Figure 3.2:** The concentration distributions of steady-state free and trapped carriers at the end of cumulative exposure of 0.5 mGy across the photoconductor layer (normalized distance = $x/L$).

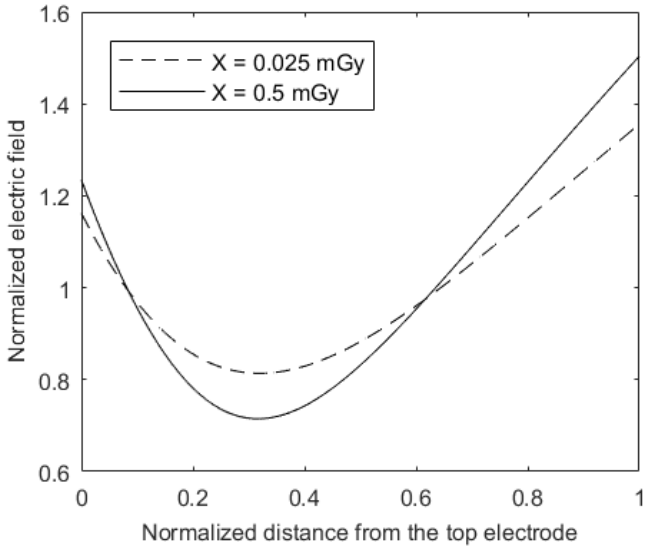


**Figure 3.3:** The normalized electric field distribution as a function of cumulative dose.

We also examine the X-ray sensitivity at a higher dose rate. Figure 3.4 shows the collected charge of an 800 μm thick $MAPbI_3$ X-ray detector as a function of X-ray dose at 70 kVp with 2.5 mm Al filtration. The average photon energy, $E_{av}$ = 42 keV, and applied electric field $F_0$ = 0.2 V/μm. The exposure time is 2 s per exposure and the dose rate is varied up to 6 $mGys^{-1}$. As a result, the total dose per exposure is varied. The open circles and dashed lines represent the experimental data and the linear fit using the analytical model of Ref. [25]. The solid and dash-dotted lines represent the model fits to the experimental data using the present numerical model and COMSOL simulation, respectively. The fitted value of deep trapping time for both electrons and holes are 350 μs [21]. The drift mobility for both electrons and holes for this detector is assumed as 2.6 $cm^2/V/s$ [21]. The experimental data were extracted from Figure 4 of Ref. [21]. The deviation of the collected charge from the linear curve represents a reduction of X-ray sensitivity with the increase of dose. Since the exposure time is the same, the sensitivity reduction is also dependent on the dose rate. There are few possible reasons for this sensitivity reduction, such as non-uniform electric field distribution and/or bim0olecular recombination between electrons and holes.

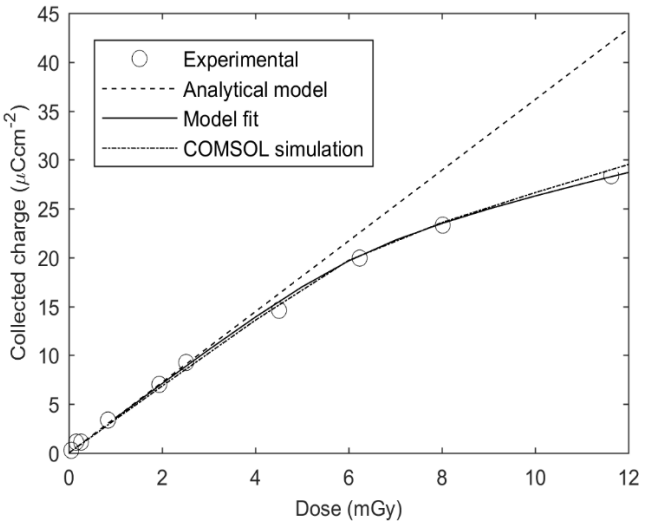


**Figure 3.4:** Collected charge as a function of dose per exposure. An 800 μm thick $MAPbI_3$ X-ray detector with applied electric field $F_0$ = 0.2 V/μm under X-ray exposure at 70 kVp with 2.5 mm Al filtration.

The trapped carrier and electric field distributions are shown in Figures 3.5 and 3.6. The dashed, solid, and dash-dotted lines in Figure 3.5 represent the trapped carrier concentrations at the end of exposures of 1, 4 and 12 mGy, respectively. As evident from Figs. 3.4 and 3.6, the difference between the dashed and solid lines in Figure 3.4 represents the reduction of X-ray sensitivity due to the non-uniform electric field. That means, the change of electric field distribution is mainly responsible for the reduction of X-ray sensitivity. The normalized electric field is getting lower than unity in the top portion of the photoconductor thickness. The photon absorption and hence the charge carrier generation rate decrease exponentially across the photoconductor thickness. The electric field becomes lower in the higher carrier generation side of the detector, which reduces the charge collection efficiency. The trapped hole concentration near the bottom electrode is much larger than the trapped electron concentration. The trapped hole concentration at the end of the highest dose (12 mGy) is close to $10^{12}$ $cm^{-3}$ across almost the entire detector thickness.

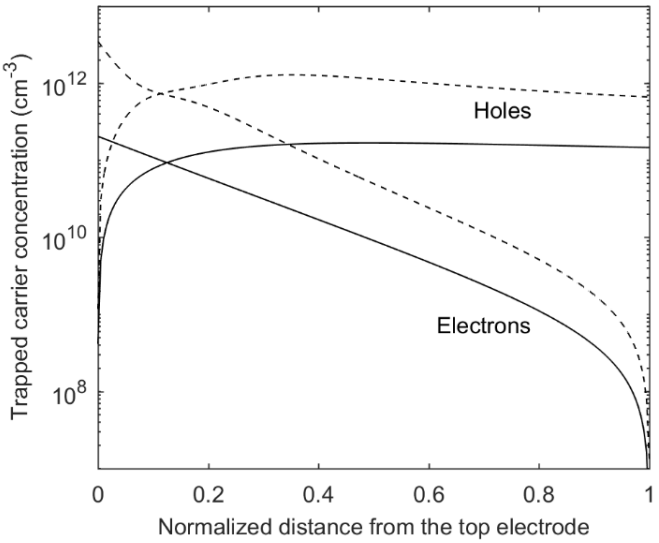


**Figure 3.5:** The trapped carrier concentrations after exposures of 1 mGy (solid lines) and 12 mGy (dashed lines). Normalized distance = $x/L$.

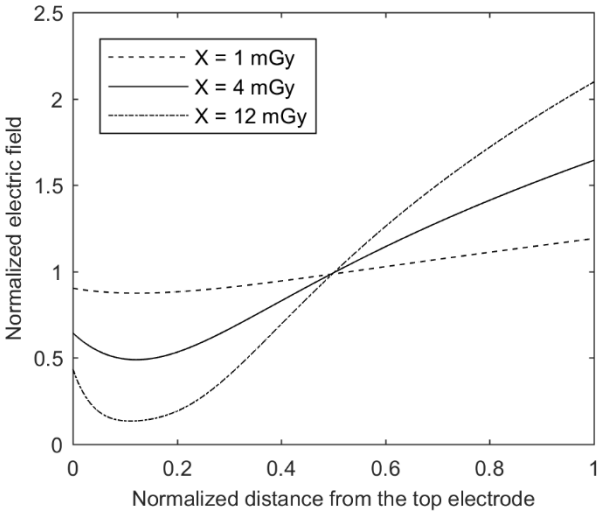


**Figure 3.6** The normalized electric field distribution as a function of dose per exposure.

The effect of the non-uniform electric field can be overcome by increasing the applied field [22] if the dark current could be controlled. The adverse effect of the non-uniform electric field increases abruptly with decreasing carrier lifetime [22]. It is also found that the effect of the bimolecular recombination between free holes and electrons on charge collection is not significantly traceable, which is consistent with previous observation in perovskite photovoltaics [32].

### 3.4 Conclusion

A numerical model for calculating the dependence of the X-ray sensitivity on the dynamics of charge carrier transport in perovskite X-ray detectors has been described. The change of sensitivity is not significant for a usual single exposure in diagnostic medical X-ray imaging applications. The electric field distribution across the photoconductor varies widely depending on operating conditions and exposure. The rapid change of electric field distribution (i.e., non-uniform electric field) mainly responsible for the reduction of X-ray sensitivity in perovskite X-ray detectors at very high exposures. The analysis in this paper will serve as a guideline for expected performance of perovskite X-ray detectors under various operating conditions.

# Chapter-4: Resolution organic perovskite X-ray detectors

## 4.1 Introduction:

In 2015, Yakunin et al. [6] first reported that a thick layer (~100 μm) of polycrystalline methylammonium lead iodide (poly-$MAPbI_3$ where MA is $CH_3NH_3$) perovskite (grain size is larger than 0.25 μm) can be uniformly deposited over large area using a solution-based synthesis technique. They measured the X-ray sensitivity and dark current of their initial prototype detector. The detector showed very good X-ray sensitivity but a very high dark current. This initial demonstration indicates that the class of Hybrid Organic−Inorganic Perovskites (HOIPs) can be used in large area X-ray imaging detectors and thus opens the door to a new class of low-cost perovskite large-area X-ray sensors [8]. Later, Kim et al. [20] proposed an innovative multilayer structure using blocking layers to poly-$MAPbI_3$ detectors to reduce the dark current. Their structure showed reasonably low dark current, good X-ray sensitivity but very poor resolution in terms of the modulation transfer function (MTF). Recently, Deumel et al. [33] reported good resolution of their 230 μm thick $MAPbI_3$ detector. Note that, until now, this was the only article that reported the measured MTF in large area perovskite X-ray detectors.

The spatial resolution of an imaging device/system is described in terms of the modulation transfer function (MTF) which is the relative response of the system as a function of spatial frequency. The flat-panel X-ray imager (FPXI) is assumed to be rotationally symmetric system, thus, the MTF is also rotationally symmetric and can be expressed in terms of single radial frequency *f*. Until now, amorphous selenium (a-Se) is the most studied and only commercially available direct conversion FPXI. The spatial resolution in a-Se FPXIs is somewhat lower than the aperture function, $MTF_a$, mainly due to the *K*-fluorescence reabsorption and charge carrier trapping in the photoconductor layer [34]. Although the carrier diffusion has a significant role on the loss of resolution, this effect is negligible in a-Se detectors because of very high applied electric field in a-Se detectors. Since the usual operating electric field in HOIP detectors is orders of magnitude lower than that in a-Se detectors [6, 20], the carrier diffusion may deteriorate the resolution significantly. It is very important to examine the quantitative effects of various possible factors that are responsible for the loss of image resolution.

In this paper, the quantitative effects of various factors (such as diffusion, *K*-fluorescence reabsorption, charge carrier trapping) that affect the resolution of HOIP detectors are examined. The effect of carrier diffusion on overall pre-sampling MTF as a function of electric field is analysed. The theoretical model calculation is compared with the published experimental data.

**4.2 The MTF model:**

The shape of pre-sampling MTF contains all the information on signal blurring of the detector, which can be described as a cascade of several independent stages where the overall MTF is simply the product of the MTFs of all the individual stages. The pre-sampling MTF of an image detector can be expressed as,

$$\mathrm{MTF}(f) = \mathrm{MTF}_g(f) \times \mathrm{MTF}_m(f) \times \mathrm{MTF}_d(f) \times \mathrm{MTF}_{tr}(f) \times \mathrm{MTF}_a(f), \qquad (4.1)$$

where $\mathrm{MTF}_m = p_{pe}\mathrm{MTF}_{pe} + p_k\mathrm{MTF}_k$ is the weighted MTF including the MTFs due to the range of the primary photoelectron and *K*-fluorescence reabsorption [35], $\mathrm{MTF}_{pe}$ is due to the range of the primary photoelectron, $\mathrm{MTF}_k$ is due to the *K*-fluorescence reabsorption, $\mathrm{MTF}_{tr}$ is due to the charge carrier trapping, and, $p_{pe,}$ and $p_k$ are the relative probabilities of the released charge carriers being from the photoelectric primary electron interaction and *K*-fluorescent x-ray reabsorption, respectively. Here, $\mathrm{MTF_d}$ and $\mathrm{MTF_g}$ are the loss of resolution due to carrier diffusion and the deviation of the X-ray incidence from the perfect perpendicular incidence. $\mathrm{MTF}_a$ is the modulation transfer function associated with the aperture function of the pixel electrodes, which describes how spatial frequencies are passed through the detector elements.

Note that the loss of resolution due to bulk trapping and carrier diffusion are not completely independent processes. Since, the amount of bulk trapping is much smaller than the blocking layer trapping, the loss of resolution due to bulk trapping alone is much smaller than that due to diffusion process in the bulk. However, the carrier diffusion is negligible as compared to carrier trapping in the blocking layer. Therefore, the carrier diffusion occurs mostly in the bulk region, whereas the carrier trapping mostly occurs in the blocking layer. As a result, they can be treated as independent processes and thus equation (4.1) can be approximated as valid.

If the aperture is a square with a dimension *a* (Figure 4.1), then,

$$\mathrm{MTF}_a(f) = \left|\mathrm{sinc}(af)\right| = \left|\frac{\sin(\pi af)}{\pi af}\right| \tag{4.2}$$

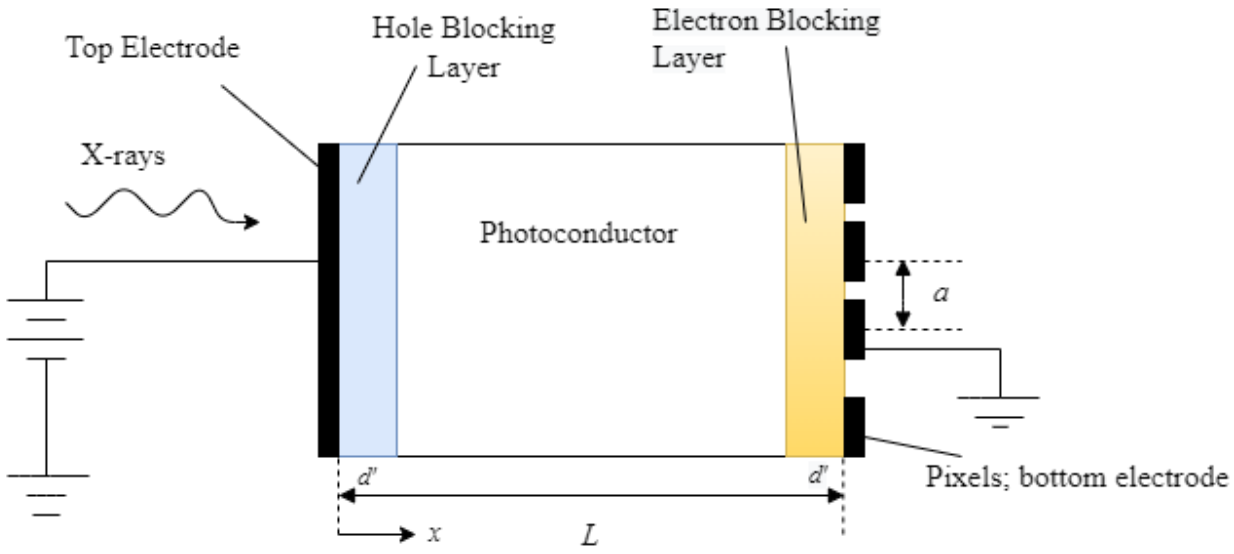


**Figure 4.1**: A schematic for the cross-sectional structure of a multilayer X-ray image detector. Here $d''$ and $d'$ are the thicknesses of the top and bottom blocking layers, respectively.

According to Que and Rowlands [33] the MTF due to the range of primary photoelectron assuming EHP generation occurs with a sphere surrounding the X-ray interaction point can be written as,

$$\mathrm{MTF}_{pe}(E, f) = \exp\left(-\pi^2\sigma^2 f^2\right), \tag{4.3}$$

where $\sigma$ is a parameter proportional to the maximum range of the primary photoelectron, $R_{\max}$. and $\sigma \approx R_{\max}/2.5$ [36]. An empirical expression for $R_{\max}$ over the energy range 10-1000 keV has been given by Kanaya and Okayama [37] that is,

$$R_{\max} = 2.761\times10^{-5} \times \frac{M_{at} E_0^{5/3}}{\rho Z^{8/9}}, \tag{4.4}$$

where $\rho$ is the density (g cm$^{-3}$), $M_{at}$ is the atomic mass (g mol$^{-1}$), $Z$ is the atomic number, $E_0$ is the energy (keV) of the primary photoelectron, and $R_{\max}$ is in mm.

The MTF due to the reabsorption of *K*-fluorescent x-ray is (in order to get the usual unity normalization of the MTF at zero frequency) [38]

$$\mathrm{MTF}_k(f) = \frac{G(f)}{G(f=0)}. \tag{4.5}$$

where,

$$G(f') = \frac{\alpha_k}{2\eta}\int_0^L \int_0^\infty \frac{e^{-\alpha_k\sqrt{r^2+\beta^2}}\left[1+e^{-\alpha\beta}-e^{-\alpha L}\left(1+e^{-\alpha\beta}\right)\right]}{r^2+\beta^2} r J_0(2\pi f' r)\, dr\, d\beta \tag{4.6}$$

$$\text{And } G(0) = \frac{\alpha_k}{2\eta}\int_0^L \int_0^\infty \frac{e^{-\alpha_k\sqrt{r^2+\beta^2}}\left[1+e^{-\alpha\beta}-e^{-\alpha L}\left(1+e^{-\alpha\beta}\right)\right]}{r^2+\beta^2} r\, dr\, d\beta \tag{4.7}$$

Here $J_0$ is the zero order Bessel function, $\eta = 1 - \exp(-\alpha L)$, $\alpha$ is the linear attenuation coefficient of incident X-rays, $\alpha_k$ is the linear attenuation coefficient of k-fluorescence X-rays.

The MTF due to the bulk carrier trapping, $\mathrm{MTF}_{tr}(E, f)$, for a monoenergetic x-ray beam under negative biased is given by [39],

$$\mathrm{MTF}_{tr}(E,f) = \frac{G'(f)}{G'(0)} \tag{4.8}$$

where,

$$G'(f) = \frac{(\tau_b+\tau_t)\left(\omega\ \mathrm{cosech}\omega - \mathrm{e}^{-\frac{1}{\Delta}}\ \omega\ \coth\omega - \Delta^{-1}\mathrm{e}^{-\frac{1}{\Delta}}\right)}{\eta\Delta^2(1-\tau_b/\Delta)\ (1+\tau_t/\Delta)\ \left(\Delta^{-2}-\omega^2\right)} - \frac{\left(\omega\ \mathrm{cosech}\omega - \mathrm{e}^{-\frac{1}{\tau_b}}\ \omega\ \coth\omega - \tau_b^{-1}\mathrm{e}^{-\frac{1}{\tau_b}}\right)}{\eta\Delta(1-\tau_b/\Delta)\ \left(\tau_b^{-2}-\omega^2\right)}$$

$$+\frac{\left(\mathrm{e}^{-\frac{1}{\Delta}-\frac{1}{\tau_t}}\ \omega\,\mathrm{cosech}\omega - \mathrm{e}^{-\frac{1}{\Delta}}\ \omega\coth\omega + \tau_t^{-1}\mathrm{e}^{-\frac{1}{\Delta}}\right)}{\eta\Delta(1+\tau_t/\Delta)\left(\tau_t^{-2}-\omega^2\right)}$$

$$+\frac{Q_b}{1-\omega^2\tau_p^2}\left\{\frac{\sinh\omega(1-d)}{\sinh\omega}+\frac{\omega\tau_p\cosh\omega(1-d)}{\sinh\omega}-e^{-d/\tau_p}\left(1+\omega\tau_p\coth\omega\right)\right\}+Q_b e^{-d/\tau_p} \tag{4.9}$$

The expression for $G(f = 0)$ is

$$G'(0)=\frac{(\tau_b+\tau_t)\ \left(1-\mathrm{e}^{-\frac{1}{\Delta}}\ -\Delta^{-1}\mathrm{e}^{-\frac{1}{\Delta}}\right)}{\eta(1-\tau_b/\Delta)\ (1+\tau_t/\Delta)}-\frac{\tau_b\left(\tau_b-\mathrm{e}^{-\frac{1}{\tau_b}}\ -\tau_b\mathrm{e}^{-\frac{1}{\tau_b}}\right)}{\eta\Delta(1-\tau_b/\Delta)}$$

$$+\frac{\tau_t\left(\tau_{\mathrm{t}}\ \mathrm{e}^{-\frac{1}{\Delta}-\frac{1}{\tau_t}}+\mathrm{e}^{-\frac{1}{\Delta}}-\tau_t\mathrm{e}^{-\frac{1}{\Delta}}\right)}{\eta\Delta\left(1+\tau_t/\Delta\right)}+Q_b\left\{(1-d)+\tau_p\left(1-e^{-d/\tau_p}\right)\right\} \tag{4.10}$$

where $d = d'/L$, $\Delta = 1/\alpha L$, $\tau = \mu\tau F/L$, $\tau_{\mathrm{p}} = \mu\tau_p F/L$ $\tau'$ is the carrier lifetime in the bulk layer, $\tau_p'$ is the carrier lifetime in the bottom blocking layer, $F$ is the electric field across the photoconductor layer, the subscript $t$ and $b$ refer to carrier types move towards the top and bottom electrodes respectively; the top electrode receives the X-ray radiation.

The MTF due to carrier diffusion in the bulk layer [36],

$$\mathrm{MTF}_d(f)=\frac{\alpha\left\{\exp\left[-4kT\pi^2f^2L/(eF)\right]-\exp(-\alpha L)\right\}}{\eta\left[\alpha-4kT\pi^2f^2/(eF)\right]} \tag{4.11}$$

Where $k$ is the Boltzmann constant and $T$ is the absolute temperature. The MTF due to deviation of the incident angle θ from the perfect perpendicular incidence on the detector is [34],

$$\mathrm{MTF}_g(f)=\frac{\left\{\left[1-\exp(-\alpha L/\cos\theta)\right]^2+4\exp(-\alpha L/\cos\theta)\sin^2(\pi fL\tan\theta)\right\}^{1/2}}{\left[1-\exp(-\alpha L/\cos\theta)\right]\left[1+(2\pi f\sin\theta/\alpha)^2\right]^{1/2}} \tag{4.12}$$

### 4.3 Results and discussions

Figure 4.2 shows the pre-sampling MTF of an 830 μm thick $MAPbI_3$ X-ray detector as a function of spatial frequency at 100 kVp X-ray irradiation. The average photon energy, $E_{av}$ = 52.4 keV, aperture width is 70 μm and an applied electric field $F_0$ = 0.06 V/μm. The radiation-receiving electrode is positively biased. The electron and hole mobilities are ~66 and 139 $cm^2/V/s$, according to the mentioned values in this article [20]. Note that the carrier mobility in polycrystalline perovskites is usually an order of magnitude lower than the mentioned values above [40]. The experimental data were extracted from Extended Data Figure 1c of Ref. [20]. The model agrees well with the experimental data. The fitted values of hole and electron lifetimes are 20 μs and 1 μs, which are within the range as mentioned in the Extended Data Figure 2 of Ref. [20]. The width of the PI-$MAPbI_3$ layer (bottom/hole blocking layer) is assumed to be 30 um and the carrier lifetime is 1 ns in this layer. The deviation of the incident angle θ is assumed to be 12° [34].

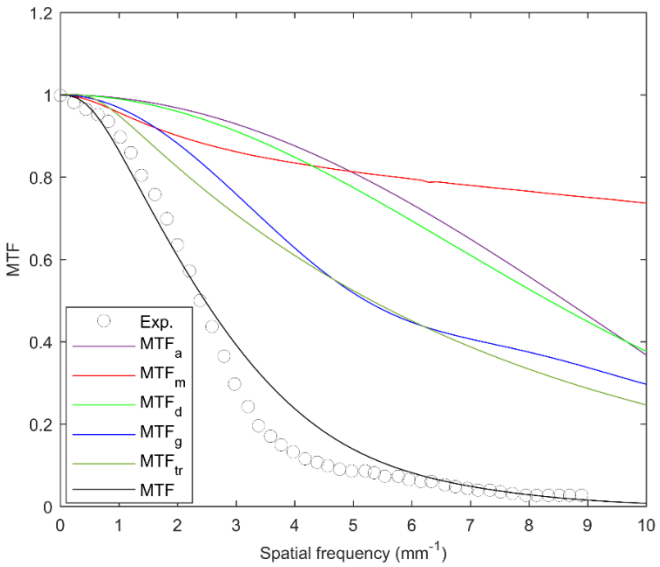


**Figure 4.2** MTF(*f*) for a positively biased and 830 μm thick $MAPbI_3$ X-ray detector at 100 kVp X-ray exposure. The applied electric field $F$ = 0.06 V/μm and the average photon energy is 52.4 keV.

The effect of carrier diffusion on MTF in $MAPbI_3$ X-ray detectors for mammographic and chest radiographic detectors are shown in Figures 4.3(a) and 4.3(b), respectively. The average photon energy and detector thickness for mammographic detectors are 20 keV and 200 μm, whereas these are 60 keV and 800 μm in chest radiographic detectors, respectively. The $MTF_d$ deteriorates abruptly with decreasing applied electric field. The effect of diffusion is more significant in chest radiographic (i.e., thicker) detectors than that in mammographic (i.e., thinner) detectors.

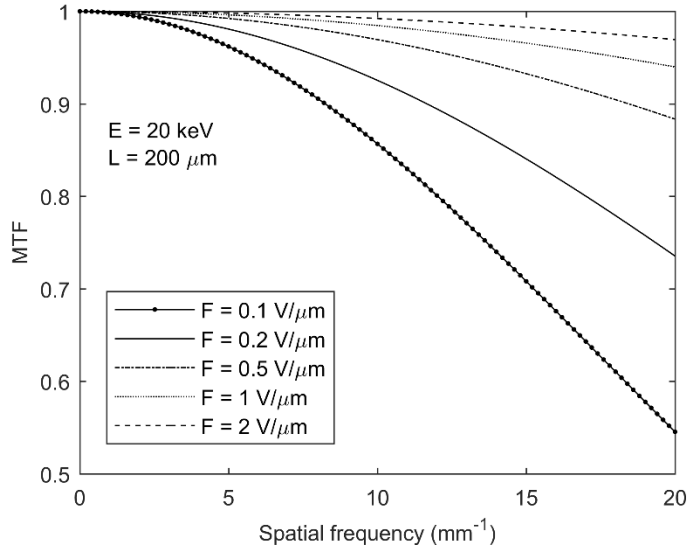


(a)

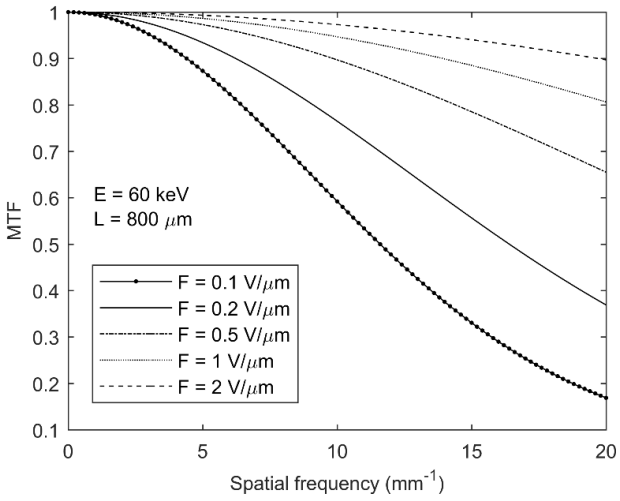


(b)

**Figure 4.3** $MTF_d$ in $MAPbI_3$ X-ray detectors for (a) mammographic and (b) chest radiographic detectors.

Figure 4.4 shows the effect of incidence angle on MTF of an 800 μm thick $MAPbI_3$ X-ray detector at 60 keV X-ray irradiation as a function of spatial frequency for various angle θ. The MTFg deteriorates abruptly with increasing the angle θ and shows a very significant effect on the pre-sampling MTF of the X-ray detector.

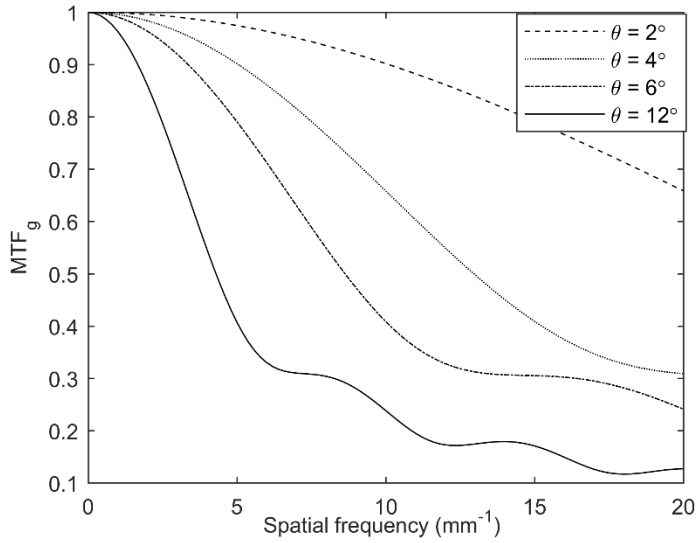


**Figure 4.4**: $MTF_g$ of an 800 μm thick $MAPbI_3$ X-ray detector at 60 keV X-ray irradiation as a function of spatial frequency for various angle θ.

### 4.4 Conclusion

A theoretical physics-based model to evaluate presampling MTF has been applied to methylammonium lead iodide. The results of the model are compared with the experimental values. The main reasons for the loss of image resolution of organic perovskite material are due to k-fluorescence reabsorption, charge carrier trapping, and carrier diffusion. The model included the MTF due to the range of primary photoelectron, k-fluorescence reabsorption, charge carrier diffusion, charge carrier trapping, deviation of X-ray incidence from the perfect perpendicular, and the modulation transfer function associated with the aperture function of the pixel electrodes has been considered. The effect of carrier diffusion affecting the presampling MTF has been investigated for mammographic and chest radiographic detectors. The charge carrier diffusion under a low applied electric field is responsible for the deterioration of presampling Modulation transfer function of methylammonium lead iodide-based X-ray detectors. It has been found that the MTF due to the charge carrier diffusion decreases significantly with reducing the applied

electric field. The MTF due to the deviation of X-ray compared to perfectly perpendicular decreases abruptly with the increase of angle of incidence and affects significantly the presampling MTF of organic X-ray detectors.

# Chapter – 5 Conclusion, Contribution and Future Works

## 5.1 Conclusion

Important X-ray detector metrices such as Sensitivity, Photocurrent, Ghosting (reduction of sensitivity under repeated exposures), Modulation transfer function MTF has been critically analyzed. Analytical models with valid assumptions have been implemented to evaluate the underlying features of signal loss during X-ray imaging. The continuity equations for both holes and electrons, the Poissons equation, and trapping rate equations with proper boundary conditions are solved simultaneous with finite difference method and results are compared with the aid of COMSOL Multiphysics. Furthermore, all the recombination mechanisms have been included with proper assumptions. Experimental results are also fitted. The spatial resolution of the imaging system was described by pre-sampling modulation transfer function MTF as product of

individual MTF models that includes primary photoelectron interaction, k-fluorescence reabsorption, charge carrier diffusion, trapping in the blocking layer, modulated transfer function associated with aperture function. The loss of MTF as a function of spatial frequency has been investigated.

From these works, we conclude the reduction of sensitivity under repeated exposures exhibited by the non-uniform electric field due to charge carrier trapping. The Hybrid-Organic-Inorganic perovskite (HOIP) have crystal defects facilitates the presence of trapped-energy centers aids photogenerated carriers to get trapped and undergo trap-assisted and bimolecular recombination. In addition, the effect of bimolecular recombination is neglected in single exposure however, under repeated and large exposure, it has been observed that the bimolecular recombination becomes prominent and partially responsible for the loss of x-ray sensitivity. The charge collection in repeated high exposure experiments deviates drastically from the analytical results which itself justifies the effect of Ghosting in Hybrid Organic Inorganic Perovskite material. The presampling MTF of organic perovskite X-ray detector deteriorates due to k-fluorescence reabsorption, charge carrier trapping and charge carrier diffusion. The k-fluorescence reabsorption may take place randomly within the detector volume which causes blurring of the image. The carrier trapped near the pixel electrode induces opposite charges to central and adjacent electrodes which causes signal spreading and loss of resolution. However, charge carrier trapped away from the pixel electrode improves the sharpness of the image. The electric field applied in organic perovskite-based X-ray

detectors are one order smaller than a-Se thus the effect of charge carrier diffusion cannot be neglected. It is found out that charge carrier diffusion is responsible for the loss of resolution in perovskite X-ray detector. The applied electric field and the length of the detector structure governs the charge carrier diffusion. The deviation of angle of incidence compared to perfect perpendicular to the detector surface also plays a vital role for the abrupt reduction in resolution in perovskite X-ray detector. It is found that, increasing the angle of incidence reduces the overall resolution of the detector.

### 5.2 Contribution

The contribution of this thesis can be summarized below:

1. The reduction of sensitivity mechanisms in perovskite X-ray detectors has been investigated.
2. Fitting numerical results with experimental results with proper physical assumptions are carried out.
3. A theoretical model for calculating the presampling MTF of perovskite X-ray detector has been proposed.
4. The effects of various factors (such as charge carrier trapping and carrier diffusion) are responsible for the loss of resolution has been analyzed.

### 5.3 Publication:

A journal paper entitled “Sensitivity reduction mechanism in organic perovskite X-ray detectors” by Afazul Hoq, D. M. Panneerselvam, and M. Z. Kabir, was published in *Journal of Materials Science: Materials in Electronics* 32.12 (2021): 16824-16830.

### 5.4 Future Works

In this thesis, the effects of diffusion of charge carriers on MTF has been critically analyzed. The results suggested that increasing the applied electric reduces charge carrier diffusion significantly and improves the presampling MTF. In the sensitivity reduction mechanism, the impact of diffusion charge carrier has been assumed to be negligible. The applied electric in perovskite detectors is relatively low as compared to other radiation detectors. In this case, the diffusion of charge carriers may play a role in charge collection. More research work is required with proper physical assumptions to investigate the effects of charge carrier diffusion on sensitivity of organic perovskite-based x-ray detector.

# References


[1] J. Beutel, et al. *Handbook of medical imaging*. Vol. 3. Spie Press, 2000.

[2] H. E. Johns and J. R. Cunningham, The physics of radiology. 4th ed. Springfield, IL: Charges C Thomas, 1983, chs. 5 and 7.

[3] "RadiologyInfo.org", Radiologyinfo.org,2017".

[4] M. Z Kabir and S.O. Kasap, "Photoconductors for Direct Conversion X-ray Image Detectors", Springer Handbook of Electronic and photonic Materials, 2nd edition, ed. By S. O. Kasap, (Springer Nature, Switzerland AG, 2017), Chapter 45

[5] S. O. Kasap and J. A. Rowlands, "X-ray photoconductors and stabilized a-Se for direct conversion digital flat panel X-ray image detectors," Journal of Materials Science: Materials in Electronics, vol. 11, no. 3, pp. 179−198, Apr. 2000.

[6] S. Yakunin, M. Sytnyk, D. Kriegner, S. Shrestha, M. Richter, G. Matt, H. Azimi, C. Brabec, J. Stangl, M. Kovalenko and W. Heiss, "Detection of X-ray photons by solution-processed lead halide perovskites", Nature Photonics, vol. 9, no. 7, pp. 444-449, 2015.

[7] H. Wei, Y. Fang, P. Mulligan, W. Chuirazzi, H. Fang, C. Wang, B. Ecker, Y. Gao, M. Loi, L. Cao and J. Huang, "Sensitive X-ray detectors made of methylammonium lead tribromide perovskite single crystals", Nature Photonics, vol. 10, no. 5, pp. 333-339, 2016.

[8] D. Panneerselvam and M. Z. Kabir, "Evaluation of organic perovskite photoconductors for direct conversion X-ray imaging detectors", Journal of Material Science: Materials in Electronics, vol. 28, pp. 7083–7090, 2017

[9] Z. Song, et al. "Pathways toward high-performance perovskite solar cells: review of recent advances in organo-metal halide perovskites for photovoltaic applications." Journal of photonics for energy 6.2 (2016): 022001.

[10] S. F. Hoefler, G. Trimmel, and T. Rath, "Progress on lead-free metal halide perovskites for photovoltaic applications", a review. *Monatsh Chem* **148,** 795–826 (2017)

[11] Z. Song, S. C. Watthage, A. B. Phillips, Michael J. Heben, "Pathways toward high-performance perovskite solar cells: review of recent advances in organo-metal halide perovskites for photovoltaic applications," J. Photon. Energy 6(2) 022001 (15 April 2016)

[12] C. A. Klein, “Bandgap dependence and related features of radiation ionization energies in semiconductors,” Journal of Applied Physics, vol. 39, no. 4, pp. 2029−2038, Mar. 1968

[13] Beutel, Jacob, Harold L. Kundel, and Richard L. Van Metter. *Handbook of medical imaging. Volume 1, Volume 1*. Bellingham, Wash: SPIE, 2000.

[14] R. A. Street, “Recombination in amorphous semiconductors,” Physical Review B, vol.17, no. 10, pp. 3984−3995, May 1978.

[15] S. Siddiquee, and M. Z. Kabir. "Modeling of photocurrent and lag signals in amorphous selenium x-ray detectors." *Journal of Vacuum Science & Technology A: Vacuum, Surfaces, and Films* 33.4 (2015): 041514.

[16] S. A. Mahmood, et al. "Investigation of ghosting recovery mechanisms in selenium X-ray detector structures for mammography." *IEEE Transactions on Nuclear Science* 59.3 (2012): 597-604.

[17] A. Hoq, D. M. Panneerselvam, and M. Z. Kabir. "Sensitivity reduction mechanisms in organic perovskite X-ray detectors." *Journal of Materials Science: Materials in Electronics* 32.12 (2021): 16824-16830.

[18] S.O. Kasap, M. Z. Kabir, and J. A. Rowlands. "Recent advances in X-ray photoconductors for direct conversion X-ray image detectors." *Current Applied Physics* 6.3 (2006): 288-292.

[19] L. Basiricò, Andrea Ciavatti, and Beatrice Fraboni. "Solution-Grown Organic and Perovskite X-Ray Detectors: A New Paradigm for the Direct Detection of Ionizing Radiation." *Advanced Materials Technologies* 6.1 (2021): 2000475.

[20] Y. C. Kim, et al. "Printable organometallic perovskite enables large-area, low-dose X-ray imaging." *Nature* 550.7674 (2017): 87-91.

[21] S. Shrestha, et al. "High-performance direct conversion X-ray detectors based on sintered hybrid lead triiodide perovskite wafers." *Nature Photonics* 11.7 (2017): 436-440.

[22] M. Z. Kabir, et al. "Sensitivity of stabilized a-Se based X-ray photoconductors." *Current Applied Physics* 6.3 (2006): 393-398.

[23] I. Cunningham, "Handbook of Medical Imaging, vol. 1." *edited by J. Beutel, H. Kundel, and RL Van Metter, SPIE, Bellingham, WA* (2000): 79.

[24] S. O. Kasap, et al. "Charge collection efficiency in the presence of non-uniform carrier drift mobilities and lifetimes in photoconductive detectors." *Journal of Applied Physics* 128.12 (2020): 124501.

[25] M. Z. Kabir, and S. O. Kasap. "Charge collection and absorption-limited sensitivity of x-ray photoconductors: Applications to a-Se and HgI 2." *Applied Physics Letters* 80.9 (2002): 1664-1666.

[26] S. A. Mahmood, and M. Z. Kabir. "Dark current mechanisms in stabilized amorphous selenium based n-i detectors for x-ray imaging applications." *Journal of Vacuum Science & Technology A: Vacuum, Surfaces, and Films* 29.3 (2011): 031603.

[27] Adinolfi, Valerio, et al. "The in-gap electronic state spectrum of methylammonium lead iodide single-crystal perovskites." *Advanced materials* 28.17 (2016): 3406-3410.

[28] Brenner, Thomas M., et al. "Hybrid organic—inorganic perovskites: low-cost semiconductors with intriguing charge-transport properties." *Nature Reviews Materials* 1.1 (2016): 1-16.

[29] M. Pope, C.E. Swenberg, Electronic Processes in Organic Crystals and Polymers, 2nd edn. (Oxford University Press, New York, 1999).

[30] Y. Chen, H.T. Yi, X. Wu, R. Haroldson, Y.N. Gartstein, Y.I. Rodionov, K.S. Tikhonov, A. Zakhidov, X.-Y. Zhu, V. Podzorov, Nat. Commun. 7, 12253 (2016)

[31] Cunningham, I. "Handbook of Medical Imaging, vol. 1." *edited by J. Beutel, H. Kundel, and RL Van Metter, SPIE, Bellingham, WA* (2000): 79.

[32] Huang, Jinsong, et al. "Understanding the physical properties of hybrid perovskites for photovoltaic applications." *Nature Reviews Materials* 2.7 (2017): 1-19.

[33] S. Deumel, et al. "High-sensitivity high-resolution X-ray imaging with soft-sintered metal halide perovskites." *Nature Electronics* 4.9 (2021): 681-688.

[34] M. Z. Kabir, et al. "Direct conversion x-ray sensors: Sensitivity, DQE and MTF." *IEE Proceedings-Circuits, Devices and Systems* 150.4 (2003): 258.

[35] Que, W., and J. A. Rowlands. "X-ray imaging using amorphous selenium: Inherent spatial resolution." *Medical physics* 22.4 (1995): 365-374.

[36] M. Z. Kabir, "Effects of charge carrier trapping on polycrystalline PbO x-ray imaging detectors." *Journal of applied physics* 104.7 (2008): 074506.

[37] Kanaya, K. A., and S. Okayama. "Penetration and energy-loss theory of electrons in solid targets." *Journal of Physics D: Applied Physics* 5.1 (1972): 43.

[38] M. Z. Kabir, M. W. Rahman, and W. Y. Shen. "Modelling of detective quantum efficiency of direct conversion x-ray imaging detectors incorporating charge carrier trapping and K-fluorescence." *IET circuits, devices & systems* 5.3 (2011): 222-231.

[39] M. Z. Kabir, "Effects of Charge Carrier Trapping on Image Resolution of Multilayer Photoconductive Detectors: Application to Amorphous Selenium X-ray Detectors." *Radiation* 2.1 (2022): 91-99.

[40] Chen, Yin, et al. "Extended carrier lifetimes and diffusion in hybrid perovskites revealed by Hall effect and photoconductivity measurements." *Nature communications* 7.1 (2016): 1-9.

# Appendix A: COMSOL simulation setup

The simulation has been carried out using COMSOL Multiphysics version 5.4 respectively.

The flowchart diagram summarizes the solution process.

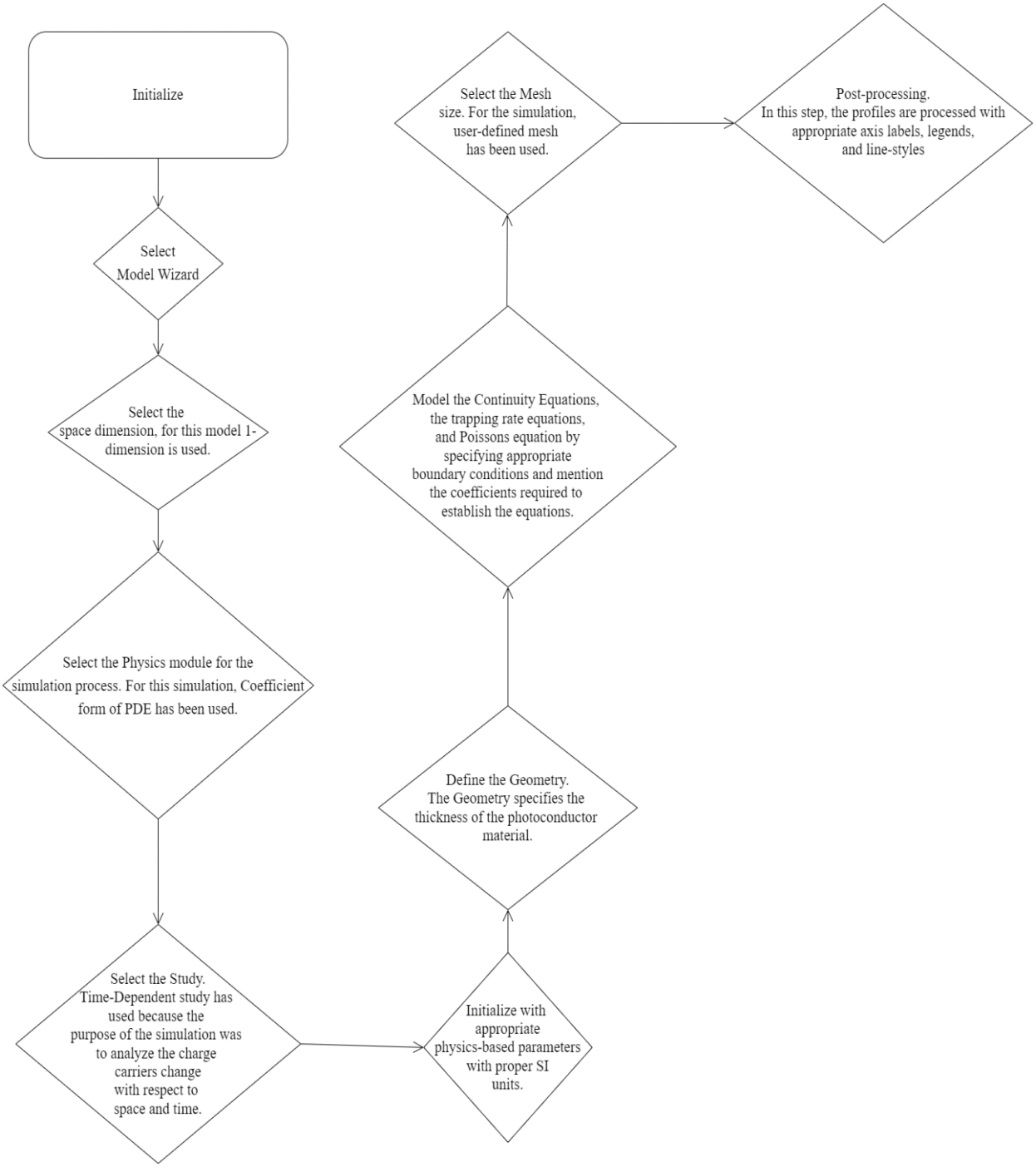

Figure A-1: The flowchart summarizes the steps and process to solve the dynamic coupled-partial differential equation to extract the various important profiles of carrier concentration, electric-field, relative sensitivity as a function of cumulative dose and charge collection as a function dose of X-ray.

The parameters and variables used in the simulations are provided in Table-1 and 2.

**Table-A.1:** Parameters for photon-energy of 52.4 KeV.

| Name | Expression | Value | Description |
|---|---|---|---|
| mue | 66[cm^2/V/s] | 0.0066 $m^2/(V \cdot s)$ | Electron-Mobility |
| muh | 139[cm^2/V/s] | 0.0139 $m^2/(V \cdot s)$ | Hole Mobility |
| Tex | 50[ms] | 0.05 s | Exposure Time |
| alpha | 39.2609[cm^-1] | 3926.1 1/m | Linear Attenuation |
| q | 1.67*10^-19[C] | 1.67E-19 C | Charge of an Electron |
| epsilon | 28*epsilon0_const | 2.4792E-10 F/m | Permittivity |
| th | 20[us] | 2E-5 s | Hole LIfetime |
| te | 20[us] | 2E-5 s | Electron Lifetime |

| | | | |
|---|---|---|---|
| G | (alpha*52.4*10^3*Photon_fluence1)/(Tex*4.5) | 5.7796E21 $1/(m^3 \cdot s)$ | Generation |
| Photon_fluence | 3.1605e10[mm^-2*Gy^-1] | 3.1605E16 $s^2/m^4$ | Photon-Fluence |
| L | 830[μm] | 8.3E-4 m | Total Thickness |
| cr | ((q*(mue+muh))/epsilon)/10 | 1.3809E-12 $m^3/s$ | Bimolecular Recombination coefficient |
| cp | cr/2 | 6.9045E-13 $m^3/s$ | Trap coefficient Relative to hole |
| cn | cr/2 | 6.9045E-13 $m^3/s$ | Trap coefficient Relative to electron |
| F | 0.06[V/um] | 60000 V/m | Electric Field |
| X | 0.2[mGy] | 2E-4 Gy | Exposure |
| Photon_fluence1 | Photon_fluence*X | 6.321E12 $1/m^2$ | Photon Fluence |

**Table-A.2:** Variables for E= 52.4 KeV.

| **Name** | **Expression** | **Unit** | **Description** |
|---|---|---|---|
| Electric Field | d(-V,x) | V/m | Electric Field |
| J_inj | e*Nv*muh*F*exp(-oe/(Kb*T)) | | Injected-current density |
| S | (Total_Hole)+(Total_Electron) | A/m² | Total Current Density |

The Partial Differential Equations are solved under the Mathematics Module, coefficient form of PDE of COMSOL Multiphysics followed by a Time-Dependent study is used to evaluate and investigate the results.

$$e_a \frac{\partial^2 n}{\partial t^2} + d_a \frac{\partial n}{\partial t} + \nabla * (-c\nabla n - \alpha n + \gamma) + \beta * \nabla n + an = \mathrm{f} \quad \text{(A.1)}$$

$$\nabla = \frac{\partial}{\partial x} \quad \text{(A.2)}$$

$$e_a \frac{\partial^2 p}{\partial t^2} + d_a \frac{\partial p}{\partial t} + \nabla * (-c\nabla p - \alpha p + \gamma) + \beta * \nabla p + ap = \mathrm{f} \quad \text{(A.3)}$$

$$\nabla = \frac{\partial}{\partial x} \quad \text{(A.4)}$$

Table A-3 Shows the different coefficient values that has been selected to design the model of Continuity Equation.

| Description | Value |
|---|---|
| Diffusion coefficient | 0 |
| Absorption Coefficient | (1/th)+(muh*(-Vxx))+(cr*n)+(cp*az) for holes, Where az is trapped-electron concentration. (1/te)-(mue*(-Vxx))+(cr*p)+(cn*bz) Where bz is trapped-hole concentration. |
| Source term | G*exp(-alpha*x)+bz/trh for hole-concentration G*exp(-alpha*x)+az/tre for electron concentration |
| Mass coefficient | 0 |
| Damping coefficient | 1 |
| Conservative Flux convection coefficient | 0 |
| Convection Coefficient | muh*Field for hole-concentration -mue*Field for electron-concentration |
| Conservative Flux source | 0 |

$$e_a \frac{\partial^2 az}{\partial t^2} + d_a \frac{\partial az}{\partial t} + \nabla * (-c\nabla az - \alpha az + \gamma) + \beta * \nabla az + \mathrm{a}az = \mathrm{f} \quad \text{(A.5)}$$

$$\nabla = \frac{\partial}{\partial x} \quad \text{(A.6)}$$

$$e_a \frac{\partial^2 bz}{\partial t^2} + d_a \frac{\partial bz}{\partial t} + \nabla * (-c\nabla bz - \alpha bz + \gamma) + \beta * \nabla bz + \mathrm{a}bz = \mathrm{f} \quad \text{(A.7)}$$

$$\nabla = \frac{\partial}{\partial x} \quad \text{(A.8)}$$

*az* represents electron-trapped and *bz* represents hole-trapped concentration.

Table A-4: Shows the different coefficient values that has been selected to design the model of Trapping-rate equation.

| Description | Value |
|---|---|
| Diffusion coefficient | 0 |
| Absorption Coefficient | cp*p+1/tre for electron-trap,<br>cn*n+1/trh for hole-trap |
| Source term | n/te for electron-trap<br>p/th for hole-trap |
| Mass coefficient | 0 |
| Damping coefficient | 1 |
| Conservative Flux convection coefficient | 0 |
| Convection Coefficient | 0 |
| Conservative Flux source | 0 |

$$\nabla * (-c\nabla \mathrm{V}) = f \quad \text{(A.9)}$$

$$\nabla = \frac{\partial}{\partial x} \quad \text{(A.10)}$$

Table A-5: The coefficient selected to model the Poisson equation.

| | |
|---|---|
| Diffusion Coefficient | 1 |
| Source Term | (q/epsilon)*((p+bz)-(n+az)) |